NEUROSCIENCE

Astrocytic dysfunction induced by ABCA1 deficiency causes optic neuropathy

Youichi Shinozaki[1,2]†, Alex Leung[3]†, Kazuhiko Namekata[4], Sei Saitoh[5,6], Huy Bang Nguyen[7,8], Akiko Takeda[1], Yosuke Danjo[1], Yosuke M. Morizawa[1], Eiji Shigetomi[1,2], Fumikazu Sano[1], Nozomu Yoshioka[9], Hirohide Takebayashi[9], Nobuhiko Ohno[10,11], Takahiro Segawa[12], Kunio Miyake[13], Kenji Kashiwagi[14], Takayuki Harada[4], Shin-ichi Ohnuma[3]*, Schuichi Koizumi[1,2]*

Astrocyte abnormalities have received great attention for their association with various diseases in the brain but not so much in the eye. Recent independent genome-wide association studies of glaucoma, optic neuropathy characterized by retinal ganglion cell (RGC) degeneration, and vision loss found that single-nucleotide polymorphisms near the ABCA1 locus were common risk factors. Here, we show that *Abca1* loss in retinal astrocytes causes glaucoma-like optic neuropathy in aged mice. ABCA1 was highly expressed in retinal astrocytes in mice. Thus, we generated macroglia-specific *Abca1*-deficient mice (Glia-KO) and found that aged Glia-KO mice had RGC degeneration and ocular dysfunction without affected intraocular pressure, a conventional risk factor for glaucoma. Single-cell RNA sequencing revealed that *Abca1* deficiency in aged Glia-KO mice caused astrocyte-triggered inflammation and increased the susceptibility of certain RGC clusters to excitotoxicity. Together, astrocytes play a pivotal role in eye diseases, and loss of ABCA1 in astrocytes causes glaucoma-like neuropathy.

INTRODUCTION

Glaucoma, a progressive optic neuropathy characterized by retinal ganglion cell (RGC) degeneration and vision loss, affects more than 70 million people worldwide (*1*). Although glaucoma is a multifactorial disease (*2*), elevated intraocular pressure (IOP) is a major risk factor, and genetic variabilities can affect disease onset and progression. Previous genome-wide association studies identified single-nucleotide polymorphisms (SNPs) of a locus near *ABCA1* as a common genetic risk factor for primary open-angle glaucoma (*3*–*6*), but the causal relationship between *ABCA1* variation and glaucoma remains unclear.

ABCA1 is a membrane protein that mediates multiple functions, including phospholipid scrambling (*7*), phagocytosis (*8*), immune-cell regulation (*9*), control of endocytosis/exocytosis (*10*), regulation of intracellular signaling (*11*), anti-inflammation (*12*), and transport of cholesterol and phospholipids to extracellular lipid-free apolipoproteins (*13*). A previous report showed that ABCA1 is highly expressed in brain astrocytes (*8*), but it remained unclear whether astrocyte-lineage cells express ABCA1 in ocular tissue. Astrocytes are a nonneuronal cell type in the central nervous system (CNS) that control CNS homeostasis, synapse formation, and synaptic function. Under pathological conditions, astrocytes adopt either neuroprotective (*14*) or neurotoxic phenotypes (*15*–*17*). Dysregulated neurotoxic astrocytes may participate in the pathogenesis of various neurodegenerative diseases (*18*). In addition to neurodegenerative diseases of the CNS, dysregulated astrocytes can cause RGC degeneration in the chronic ocular hypertension model (*19*), a widely used glaucoma model.

Astrocytes in the normal retina localize at the innermost surface, whereby they form a mesh-like network in various species, including rodents (*20*), pigs (*21*), monkeys (*22*), and humans (*23*). Their endfeet tightly contact blood vessels and RGC axons. In addition to the retina, astrocytes are highly enriched in the optic nerve head (ONH) of mice (*24*), monkeys (*25*), and humans (*26*). The ONH is one of the most sensitive and vulnerable parts of the ocular tissue during glaucoma pathogenesis (*27*). In the various species mentioned above, ONH astrocytes form a glial tube in the glial lamina [lamina cribrosa–like glial structure without extracellular matrix plate (*24*)] through which axons form paths and provide neurotrophic and homeostatic support. In patients with glaucoma, ONH astrocytes change their hypertrophy and morphology (*28*) and induce tissue remodeling that reduces structural support for axons. Such astrocytic changes are one of the earliest events occurring in animal models of glaucoma, often observed before axonal damage (*29*). The possibility that astrocyte dysfunction is important in the development of glaucomatous optic neuropathy suggests a previously unidentitied therapeutic strategy for glaucoma. In the present study, we addressed four issues. First, it is still unknown whether gain of neurotoxicity or loss of function of ABCA1 is important for the pathogenesis of glaucoma. Second, previous reports showed that SNPs at a locus near *ABCA1* are associated with higher risks for both normal-tension glaucoma (NTG) and hypertensive glaucoma. If *ABCA1* is indeed a causal gene of glaucoma, it is unclear whether high IOP is required for glaucoma progression and whether ABCA1 loss of function triggers high

[1]Department of Neuropharmacology, Interdisciplinary Graduate School of Medicine, University of Yamanashi, Yamanashi, Japan. [2]GLIA Center, University of Yamanashi, Yamanashi, Japan. [3]UCL Institute of Ophthalmology, University College London, London, UK. [4]Visual Research Project, Tokyo Metropolitan Institute of Medical Science, Tokyo, Japan. [5]Section of Electron Microscopy, Supportive Center for Brain Research, National Institute for Physiological Sciences (NIPS), Aichi, Japan. [6]Department of Anatomy II and Cell Biology, Fujita Health University School of Medicine, Aichi, Japan. [7]Division of Neurobiology and Bioinformatics, NIPS, Aichi, Japan. [8]Department of Anatomy, Faculty of Medicine, University of Medicine and Pharmacy (UMP), Ho Chi Minh City, Vietnam. [9]Division of Neurobiology and Anatomy, Graduate School of Medical and Dental Sciences, Niigata University, Niigata, Japan. [10]Division of Ultrastructural Research, NIPS, Aichi, Japan. [11]Department of Anatomy, Jichi Medical University, Tochigi, Japan. [12]Center for Life Science Research, University of Yamanashi, Yamanashi, Japan. [13]Department of Health Sciences, Interdisciplinary Graduate School of Medicine, University of Yamanashi, Yamanashi, Japan. [14]Department of Ophthalmology, Interdisciplinary Graduate School of Medicine, University of Yamanashi, Yamanashi, Japan.
*Corresponding author. Email: skoizumi@yamanashi.ac.jp (S.K.); s.ohnuma@ucl.ac.uk (S.-i.O.)
†These authors contributed equally to this work.

IOP. Third, although previous data provided spatial patterns of ABCA1 expression, it is unclear which cell types express ABCA1 in ocular tissue. Accordingly, the cell type that triggers ABCA1-associated glaucoma is unknown. Fourth, the retina has many RGC subtypes (*30*, *31*), and little is known about which RGC subtypes are sensitive to glaucoma. Thus, the identification of glaucoma-sensitive RGCs can contribute to the development of treatments for glaucoma.

RESULTS

ABCA1 loss caused age-associated RGC degeneration

We first examined the effect of ABCA1 deficiency on the viability of RGCs in 3-month-old (3-mo) conventional *Abca1*-knockout (KO) mice but found no changes in numbers of Brn3a-positive (Brn3a$^+$) RGCs (Fig. 1A). Previous studies suggested that aging is required for RGC degeneration (*32*, *33*). KO mice at 12 months showed a slight but significant reduction in RGC numbers (Fig. 1B). In addition, numbers of apoptotic cells detected by terminal deoxynucleotidyl transferase–mediated deoxyuridine triphosphate nick end labeling (TUNEL) in the ganglion cell layer (GCL) were significantly increased in 12-mo KO mice (Fig. 1C), while apoptotic signals were only faintly detectable in wild-type (WT) mice. TUNEL signals were colocalized with Brn3a (Fig. 1D). Retinal slices from 12-mo KO mice exhibited apoptotic signals in layers other than the GCL, including the inner and outer nuclear layers (INL and ONL, respectively) (fig. S1A).

Next, we explored the role of ABCA1 in IOP regulation, a major risk factor for glaucoma. KO mice did not exhibit higher IOP than WT mice (Fig. 1E). Because measurements of IOP values by rebound tonometry can be affected by central corneal thickness (CCT), we also performed z-stack imaging of corneas and found no corneal structural abnormalities or CCT changes in KO mice (fig. S1, B and C). These findings indicate that *Abca1* deletion caused degeneration of RGCs that was not caused by high IOP.

ABCA1 was enriched in astrocytes of the retina, ONH, and optic nerve

We next investigated the identities of cell types expressing ABCA1. Magnetic cell separation of retinal cells (fig. S2) obtained from 3-mo WT mice revealed that *Abca1* mRNA was enriched in the ACSA1$^+$ fraction (astrocytes and Müller cells) (Fig. 2A). Specifically, *Abca1* mRNA levels in the ACSA1$^+$ fraction were 3.5-fold higher than observed in CD11b$^+$ (microglia) or ACSA1-negative fractions (containing neurons, pericytes, endothelial cells, and other cell types). In situ hybridization of the retina from 3-mo WT mice showed that *Abca1* mRNA was also enriched in the nerve fiber layer (NFL), where astrocytes are present, as well as other neural layers (Fig. 2B). Immunofluorescence images of retinal sections from 3-mo WT mice revealed ABCA1 signals in the NFL (Fig. 2C and fig. S3A), reproducing previous reports of human retina (*3*, *4*). ABCA1 colocalized with signals for glial fibrillary acidic protein (GFAP), a marker for astrocytes (Fig. 2, C to E). In contrast, strong ABCA1 signals were not colocalized with signals for vimentin, a marker for Müller cells (Fig. 2D and fig. S3B). Weak ABCA1 signals observed adjacent to the endfeet of Müller cells (Fig. 2E) indicated that ABCA1 was highly expressed in astrocytes. The human retina also exhibited colocalization of ABCA1 with GFAP in the NFL (Fig. 2F). Because a previous study of human ocular tissue observed much higher ABCA1 signals in glial columns of the optic nerve (ON) (*4*), we next investigated

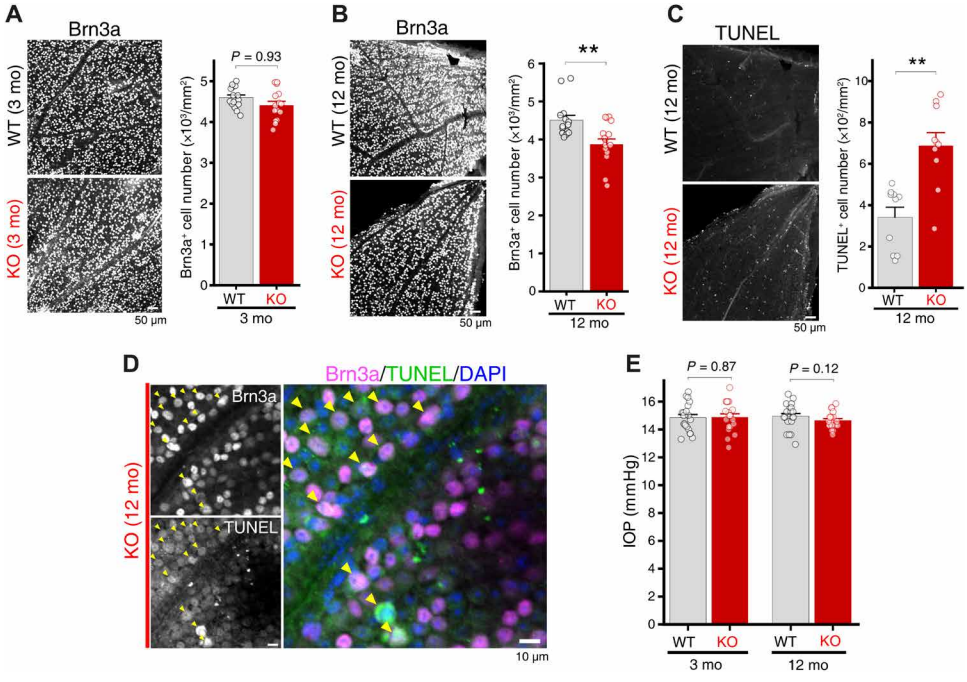

Fig. 1. ABCA1 deficiency caused age-associated RGC degeneration. (**A** and **B**) Brn3a signals in retinae from WT and KO mice at 3 and 12 months of age (3 and 12 mo, respectively). (A) At 3 mo, numbers of Brn3a$^+$ cells did not differ between WT and KO mice (n = 15 retinae, P = 0.93, Mann-Whitney U test). (B) At 12 mo, Brn3a$^+$ cell numbers in KO mice were reduced compared with those in WT mice (n = 15, $^{**}P < 0.01$, Mann-Whitney U test). (**C**) TUNEL$^+$ cell numbers were significantly higher in 12-mo KO mice compared with those in WT mice (n = 10, $^{**}P < 0.01$, Mann-Whitney U test). (**D**) TUNEL and Brn3a signals were colocalized (arrowheads), and TUNEL$^+$/Brn3a$^+$ cells were abundant in KO mice. (**E**) KO mice showed no changes in intraocular pressure (IOP; n = 20 eyes, Mann-Whitney U test). Data represent means ± SEM.

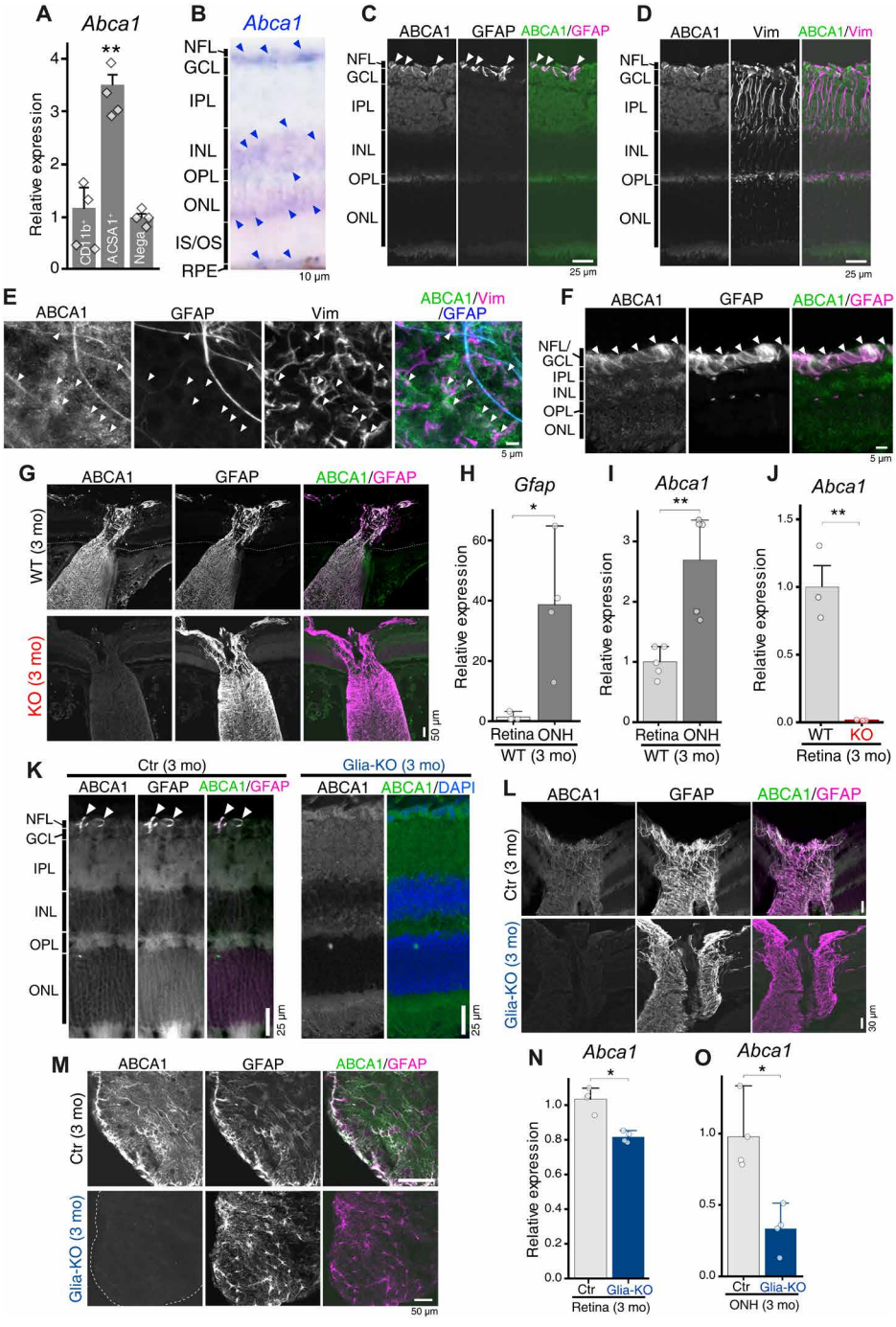

Fig. 2. ABCA1 was expressed in astrocytes. (**A**) Expression levels of *Abca1* mRNA in CD11b$^+$ (microglia), ACSA1$^+$ (astrocytes/Müller cells), and negative retinal fractions were evaluated. The ACSA1$^+$ fraction exhibited 3.5-fold higher *Abca1* levels ($n = 4$ tissues, $^{**}P < 0.01$ versus Nega; one-way analysis of variance followed by Fisher's least significant difference test). (**B**) In situ hybridization. Relatively higher levels of *Abca1* mRNA (blue signal) were detected at the inner surface of the retina, with some expression in the INL and ONL in 3-mo WT mice. (**C** and **D**) ABCA1 protein expression patterns in retinal slices of 3-mo WT mice. ABCA1 signals colocalized with GFAP (arrowheads) but not vimentin (Vim). (**E**) In flat-mount retinae, strong ABCA1 signals colocalized with GFAP, while relatively weak ABCA1 signals surrounded Vim$^+$ Müller cell endfeet (arrowheads). (**F**) ABCA1 was also expressed in GFAP$^+$ astrocytes of human retinae. (**G**) The ONH showed substantially higher ABCA1 signals that were colocalized with GFAP. ABCA1 signal intensity was reduced in KO mice. (**H** and **I**) Similar to immunohistochemistry, both (H) *Gfap* and (I) *Abca1* mRNA levels were significantly higher in the ONH compared with those in the retina. (**J**) *Abca1* mRNA was absent in KO mice. (**K** to **M**) ABCA1 expression in Ctr and Glia-KO mice. ABCA1 was detected in astrocytes of 3-mo Ctr mice, while strong ABCA1 signals were not observed in Glia-KO mice. (L and M) ABCA1 signals were also observed in astrocytes in the ONH and ON but absent in Glia-KO mice. Glia-KO mice exhibited (**N**) ~20% and (**O**) ~70% reductions in *Abca1* mRNA in the retina and ONH, respectively. Data represent means ± SEM. NFL, nerve fiber layer; GCL, ganglion cell layer; IPL, inner plexiform layer; INL, inner nuclear layer; OPL, outer plexiform layer; ONL, outer nuclear layer; IS/OS, inner and outer segment; RPE, retinal pigment epithelium. H: ($n = 4$ tissues, $^*P < 0.05$, Mann-Whitney *U* test), I: ($n = 5$ tissues, $^{**}P < 0.01$, Mann-Whitney *U* test), J: ($n = 3$ retinae, $^{**}P < 0.01$, Mann-Whitney *U* test), N: ($n = 4$ retinae, $^*P < 0.05$, Mann-Whitney *U* test), O: ($n = 4$ tissues, $^*P < 0.05$, Mann-Whitney *U* test).

ABCA1 expression in the ONH and ON. ABCA1 signals were substantially higher in the ONH and ON, which were highly enriched in GFAP (Fig. 2G). Supporting this observation, *Abca1* and *Gfap* mRNA levels were significantly higher in the ONH compared with those in the retina (Fig. 2, H and I). In contrast to WT mice, KO mice showed no ABCA1 immunofluorescence signals or *Abca1* mRNA expression (Fig. 2, G and J). To investigate the role of ABCA1 in astrocytes, we crossed ABCA1$^{flox/flox}$ mice with GFAP-Cre mice to knock down *Abca1* under control of the *Gfap* promoter. In the retina, the *Gfap* promoter is active in both astrocytes and Müller cells, so we designated this conditional KO mouse as "Glia-KO." Littermate ABCA1$^{flox/flox}$ mice were used as a control (referred to as Ctr mice). Strong ABCA1 signals in Ctr mice (3 months) retinae showed fibrous patterns in the NFL and GCL, as seen in WT mice (Fig. 2K). These signals colocalized with GFAP in Ctr mice but were absent in Glia-KO mice (fig. S3, C and D). In the ONH, ABCA1 signals accumulated and colocalized with GFAP in Ctr mice but were absent in Glia-KO mice (Fig. 2L). Horizontal sections of ON from Ctr mice (3 months) also showed a fibrous pattern of ABCA1 colocalized with GFAP (Fig. 2M), but no ABCA1 signals were observed in 3-mo Glia-KO mice. Glia-KO mice showed approximately 20 and 60% reductions in *Abca1* mRNA expression in the retina and ON, respectively (Fig. 2, N and O). Collectively, these results suggest that ABCA1 is highly expressed by astrocytes in ocular tissue.

Astrocytic ABCA1 loss caused age-associated RGC degeneration without IOP changes

We next asked whether a deficiency of astrocytic ABCA1 can cause RGC degeneration. Similar to KO mice, 3-mo Glia-KO mice showed no changes in numbers of Brn3a$^+$ RGCs (Fig. 3A) or apoptotic cells (Fig. 3B). However, 12-mo Glia-KO mice showed a moderate (~20%) but significant reduction in numbers of RGCs (Fig. 3C) and increased numbers of TUNEL$^+$ cells (Fig. 3D). RGC loss was further exacerbated (~30%) in 18-mo Glia-KO mice (Fig. 3E). Reductions in RGC numbers were further confirmed by evaluating the expression of Rbpms, another marker for RGCs (fig. S4, A and B). Unlike KO mice, apoptotic signals were limited to the GCL and never observed in other neural layers (fig. S4C). Glia-KO mice (12 months) showed accumulation of cholesterol, a substrate of ABCA1, in the NFL where astrocytes are present (fig. S4, D and E). In the GCL and inner plexiform layer (IPL), where RGCs soma and dendrites are present, the cholesterol content of Glia-KO mice was lower than that of Ctr mice (fig. S4F). Consistent with these observations, cholesterol efflux in the aqueous humor of Glia-KO mice was markedly reduced (fig. S4G). No changes in CCT (fig. S4, H and I) or IOP (Fig. 3F) were observed in Glia-KO mice. Thus, our results show that the RGC degeneration observed in KO mice was mainly caused by astrocytic ABCA1 loss in an IOP-independent manner.

Glia-KO induced optic neuropathy–like phenotypes

RGC damage is associated with thinning of the NFL, GCL, and IPL, which can be observed in patients with glaucoma (*34*). In this study, optical coherence tomography analysis revealed significant thinning of the inner retinal layers in 12-mo Glia-KO mice (Fig. 4A). The reduction of excitatory synapses in the IPL is a feature of RGCs in animal models of glaucoma (*35*). Consistent with previous studies, Glia-KO retinae (12 months) showed reductions in PSD95 levels in the IPL (Fig. 4B). A previous study also reported the presence of swollen axons in a nonhuman primate glaucoma model (*27*). To test this, we performed serial block-face scanning electron microscopy (SBF-SEM) to analyze axonal structures (fig. S4, J to L), which revealed that Glia-KO axons were swollen because of accumulated membranous organelles (Fig. 4, C to E). Such axonal swelling was also revealed by Tuj1 signals in horizontal ON slices of 12-mo Glia-KO mice (Fig. 4F), consistent with observations in glaucoma model mice (*24*, *36*). The ONH is known to be the site of axonal damage in rodent (*36*) and primate (*37*) models of glaucoma, as well as patients with glaucoma (*28*). To test this, we estimated axonal damage in vertical ONH sections. We found that Ctr mice (12 months) exhibited a strong and uniform Tuj1 signal in the NFL of the retina, ONH, and ON, but this signal ended at the glial lamina in Glia-KO mice (12 months) (Fig. 4F), consistent with previous results (*36*). In addition, axons in vertical ON sections of Glia-KO mice were unevenly distributed and showed regional loss similar to patients with glaucoma (*38*). To test whether these histological changes in Glia-KO mice were relevant to visual functions, we performed multifocal electroretinograms (mfERG) because the activity of RGCs contributes to mfERG responses in mice (*39*), monkeys (*40*), and humans (*41*). The second-order kernel of mfERG is a sensitive indicator of inner retinal dysfunction (*42*) and impaired in patients with glaucoma (*43*). Accordingly, we measured the amplitude of second-order kernel responses of Ctr and Glial-KO mice. Three-dimensional plots of these responses demonstrated that the reduction in responses of Glia-KO mice (12 months) occurred unevenly (Fig. 4G). Averaged second-order kernel responses from 10 eyes demonstrated that the responses of Glia-KO mice were reduced by almost half compared with those of age-matched Ctr mice. Therefore, our results show that ABCA1 deficiency, especially in astrocytes, caused optic neuropathy–like phenotypes.

Deletion of *Abca1* caused age-associated changes in astrocyte hypertrophy

Because changes in astrocyte hypertrophy are often associated with CNS disorders and diseases, we next investigated astrocyte hypertrophy in Glia-KO mice. Glia-KO mice (3 months) exhibited increased GFAP immunofluorescence signals in both flat-mount and sliced retinae (Fig. 5, A and B) but no changes in *Gfap* mRNA levels in the retina (Fig. 5C). However, at 12 months, the Glia-KO retina exhibited rather decreased GFAP signals and *Gfap* mRNA expression (Fig. 5, D to F). We next investigated astrocytic hypertrophy in the glial lamina of the ONH (Fig. 5G). At 3 months, the ONH of Glia-KO mice showed stronger GFAP signals (Fig. 5H) and higher *Gfap* mRNA expression compared with that of Ctr mice (Fig. 5I). At 12 months, both GFAP signal and *Gfap* mRNA expression in the Glia-KO ONH were decreased compared with those in age-matched Ctr mice (Fig. 5, J and K).

Bulk and single-cell RNA sequencing revealed astrocyte-triggered inflammation

To further clarify the detailed mechanisms underlying how astrocytic ABCA1 loss causes optic neuropathy-like phenotypes, we performed single-cell RNA sequencing (scRNA-seq) (all cell types from 12-mo WT and KO mice) and bulk RNA-seq of whole retinae (12-mo Ctr and Glia-KO mice) (fig. S5A). Ingenuity Pathway Analysis (IPA) revealed that most up-regulated canonical pathways (CPs) were shared between KO and Glia-KO mice (Fig. 6A). In addition, many annotations identified for Disease or Function Annotation (DFA) analysis were common between the two groups, such as "Retinal

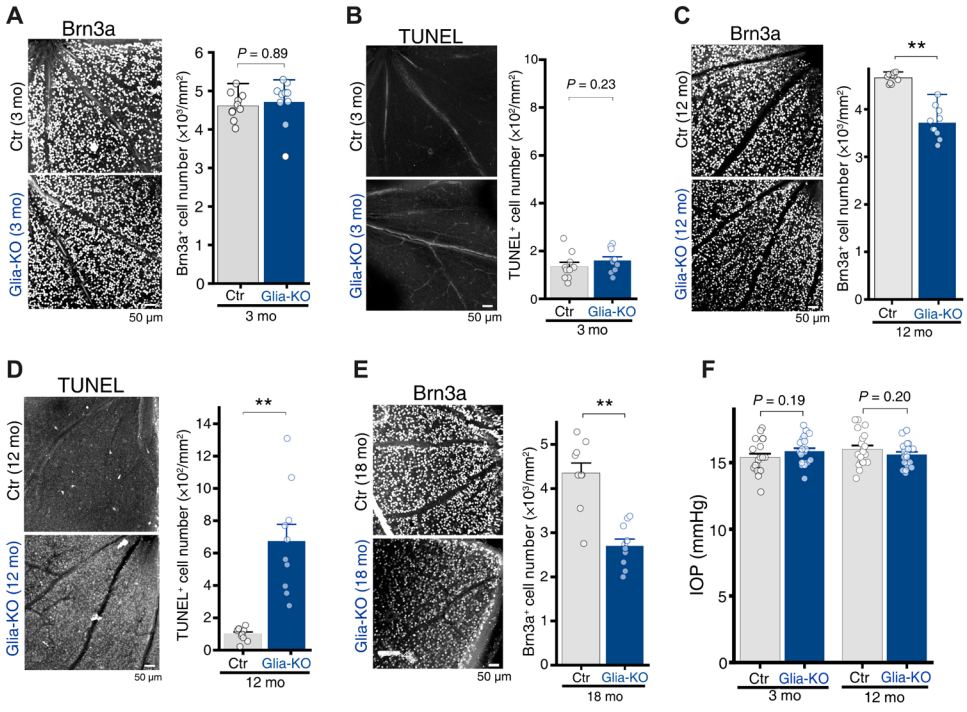

Fig. 3. ABCA1 loss in astrocytes resulted in age-associated RGC degeneration. At 3 mo, Glia-KO mice showed (**A**) no reduction in Brn3a$^+$ cells and (**B**) no increase in TUNEL$^+$ cells compared with Ctr mice (n = 10 retinae, P = 0.89 and 0.23 for Brn3a and TUNEL, Mann-Whitney U test). Glia-KO mice at 12 mo exhibited (**C**) reduced numbers of RGCs and (**D**) increased apoptotic cell numbers (n = 10 retinae, $^{**}P < 0.01$, Mann-Whitney U test). (**E**) RGC loss was greater in Glia-KO mice at 18 mo (n = 10 retinae, $^{**}P < 0.01$, Mann-Whitney U test). (**F**) Glia-KO mice showed no IOP changes compared with age-matched Ctr mice (n = 20 eyes, Mann-Whitney U test). Data represent means ± SEM.

degeneration" and "Hereditary retinal disease" (fig. S5, B and C). Shared CPs also included up-regulation of inflammatory pathways, such as "CXCR4 signaling," "CCR3 signaling," "interleukin-8 (IL-8) signaling," "IL-3 signaling," and "CCR5 signaling" (Fig. 6B). These results indicate that KO and Glia-KO retinae undergo similar changes to related pathological conditions, including inflammation.

Cell type–specific profiles identified by scRNA-seq

To further examine cellular and molecular mechanisms, we used the Seurat pipeline to perform cell type–specific analysis of scRNA-seq data of retinae from 12-mo WT and KO mice. The results were confirmed immunohistochemically using age-matched Ctr and Glia-KO mice. Graph-based clustering of retinal cells based on their transcriptomes identified 32 clusters containing the following cell types: rod and cone photoreceptors, astrocytes and Müller cells, microglia and macrophages, retinal pigmented epithelial cells, bipolar cells (BCs), endothelial cells, RGCs, and other cell types (Fig. 6, C and D, and figs. S6 and S7). Significantly up-regulated RGC-specific pathways in KO retinae compared with WT retinae included inflammation, immune cell functions, oxidative stress, neurotransmitters, and metabolic pathways (fig. S8). Certain pathways up-regulated in RGCs were shared with astrocytes, such as oxidative stress (Fig. 6E). A recent study demonstrated that monoamine oxidase b (MAOB)–mediated H_2O_2 production by astrocytes causes neurodegeneration (*15*). We examined MAOB-related gene expression and found that these genes were up-regulated in the ONH of Glia-KO mice at 3 months but down-regulated at 12 months (fig. S9). We also identified several astrocyte-specific pathways including "peroxisome proliferator–activated receptor α/retinoid X receptor α activation" (Fig. 6F), which is essential for ABCA1-mediated cholesterol metabolism (*44*). Among pathways common between astrocytes and RGCs, inflammatory-related pathways were prominent, such as "High-Mobility Group Box-1 protein (HMGB1) Signaling", "Pattern Recognition Receptors (PRRs)", and "nuclear factor κB (NF-κB) activation" (Fig. 6G). CXCR4 signaling was the most substantial pathway affected in both RGCs and astrocytes. CXCL12, a ligand of CXCR4, was expressed in astrocytes and up-regulated in 12-mo Glia-KO mice (Fig. 6, H to J). CXCL12 was also expressed and up-regulated in primary cultured ON astrocytes isolated from KO mice (Fig. 6K). Both CCR3 and CCR5 signaling pathways were up-regulated in the retina (Fig. 6B) and RGCs (fig. S8A). CCL5, a ligand of CCR3 and CCR5, was expressed in astrocytes and up-regulated in 12-mo Glia-KO mice (Fig. 6, L to N). Expression and up-regulation of CCL5 were reproduced in cultured ON astrocytes (Fig. 6O). CXCR4 and CCR5 were expressed in Rbpms$^+$ RGCs regardless of mouse genotype (i.e., Ctr or Glia-KO) (Fig. 6, P and Q). Thus, our results show that ABCA1 deficiency triggered astrocyte-initiated inflammation.

Abca1 deletion–sensitive RGCs

The retina has many RGC subtypes (*30*, *31*); however, little is known about which subtypes are sensitive to glaucoma. To examine the diversity of RGC subtypes, we performed supervised clustering. This approach identified two distinct populations of RGCs (Fig. 7A), as shown in t-distributed stochastic neighbor embedding plots (Fig. 7B). Both RGC subclasses expressed pan-RGC markers (Fig. 6D). One of the two RGC subclasses (RGC-1) was significant reduced in number in KO mice (Fig. 7, C to E). RGC-1 exhibited enrichment of DFA

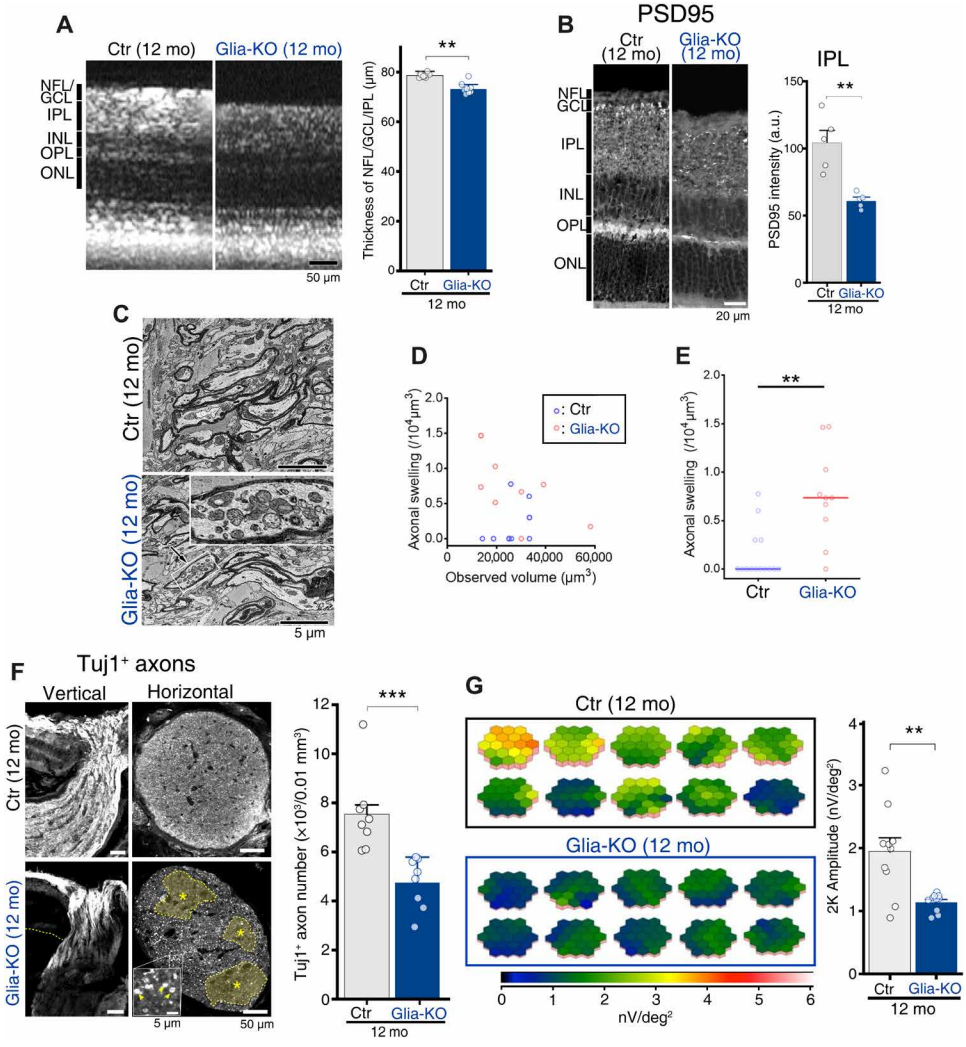

Fig. 4. Loss of ABCA1 in astrocytes triggered optic neuropathy-like pathology. (**A**) Optical coherence tomography showed NFL, GCL, and IPL thinning in 12-mo Glia-KO mice ($n = 10$ eyes, $^{**}P < 0.01$, Mann-Whitney *U* test). (**B**) PSD95 signal intensities were significantly reduced in the IPL of 12-mo Glia-KO mice ($n = 5$, $^{**}P < 0.01$, Mann-Whitney *U* test). (**C** to **E**) Serial block-face scanning electron microscopy analysis of RGC axons. Compared with Ctr ONs, Glia-KO ONs showed prominent axonal swelling caused by membranous organelle accumulation (C, arrow). Axonal swelling was greater in Glia-KO mice (D and E; $n = 10$ ONs, $^{**}P < 0.01$, Mann-Whitney *U* test). (**F**) To test axonal injury, Tuj1 signals were estimated in (left) a vertical section of the ONH and (right) a horizontal section of the ON. (Left) In the vertical section of Glia-KO ONH, Tuj1 signals ended at the myelination-transition zone. (Right) In the horizontal section of ON, regional loss of Tuj1$^+$ RGC axons was observed (asterisks). Many of the remaining axons exhibited swelling (arrowheads, inset) ($n = 8$ ONs, $^{***}P < 0.001$, Mann-Whitney *U* test). (**G**) Impaired ocular function estimated by multifocal electroretinograms. (Left) Three-dimensional plots showing averaged visual responses of the second-order kernel (2K amplitude). (Right) Ocular responses in 12-mo Glia-KO mice were significantly reduced compared with those in Ctr mice ($n = 10$ eyes, $^{**}P < 0.01$, Mann-Whitney *U* test). Data represent means ± SEM. a.u., arbitrary units.

terms "Retinal degeneration" and "Apoptosis," as well as neuropathy-related terms "Alzheimer's disease" and "Huntington's disease" (fig. S10A), indicating disease-associated changes. To obtain further insight into the underlying molecular mechanisms, we performed Kyoto Encyclopedia of Genes and Genomes analysis (*45*). RGC-1 showed enrichment of genes in the glutamatergic synapse pathway, including *Grin3a* (Fig. 7F), but less enrichment of other subtypes (including *Gria2*, *Gria3*, and *Grin2b*) and GABAergic synaptic pathway genes (Fig. 7G). RGC-1 in KO mice exhibited significantly reduced *Grin3a* gene expression (Fig. 7H). NR3A was expressed in Rbpms$^+$ RGCs (Fig. 7I), as previously reported (*46*). Quantification of RGCs with strong NR3A signals in the soma revealed that approximately 25% of RGCs expressed NR3A in 12-mo Ctr mice, but this percentage was significantly reduced in Glia-KO mice (Fig. 7, J and K). Because NR3A-containing *N*-methyl-D-aspartate (NMDA) receptors are relatively impermeable to Ca^{2+} (*47*), reduction of *Grin3a*/NR3A causes Ca^{2+} overflow (*46*) and promotes the death of RGCs (*48*). Notably, DFA analysis also identified the terms "Seizures" and "Epilepsy," supporting the possibility of glutamate excitotoxicity in RGC-1. Associated with this observation, neuronal survival– and axogenesis-related pathways (e.g., cyclic adenosine 3′,5′-monophosphate and Ras signaling) were down-regulated in KO RGC-1 (fig. S10B). In addition to the cell-autonomous mechanism, astrocytes may also contribute to non–cell-autonomous excitotoxicity in RGCs. Cultured KO astrocytes showed increased extracellular glutamate levels (fig. S10C), so ABCA1 loss may enhance glutamate release or reduce

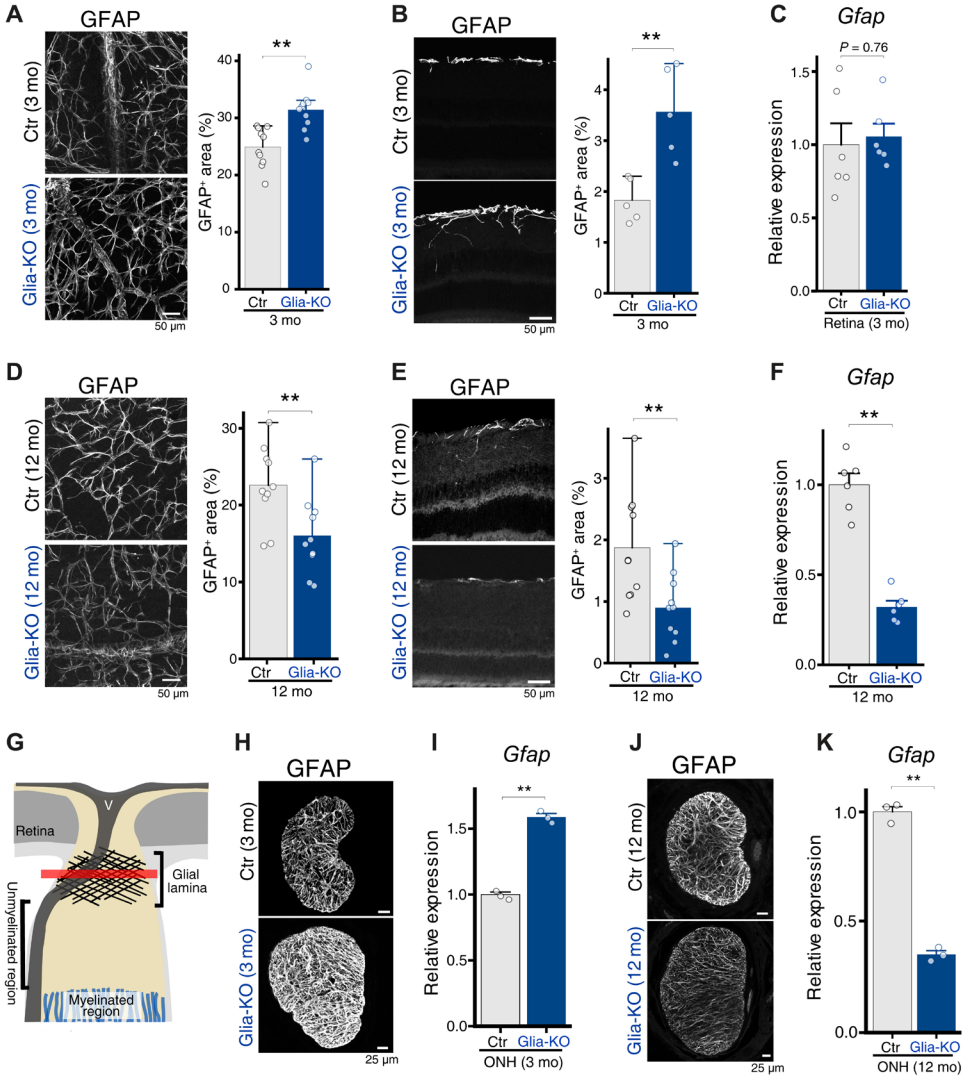

Fig. 5. Age-associated changes in retinal astrocytic hypertrophy in Glia-KO mice. (**A** and **B**) At 3 mo, the GFAP$^+$ area was larger in Glia-KO mice compared with that in Ctr mice in both (A) flat-mount and (B) sliced retinae (n = 10 and 5 for flat-mount and sliced retinae, respectively; $^{**}P < 0.01$, Mann-Whitney U test). (**C**) Retinal *Gfap* mRNA level at 3 mo was not different between Ctr and Glia-KO mice (n = 6, Mann-Whitney U test). (**D** to **F**) At 12 mo, GFAP$^+$ area and *Gfap* mRNA levels were smaller in Glia-KO mice compared with Ctr mice (n = 10, 5, and 6 for flat-mount, sliced retinae, and whole retinae, respectively. $^{**}P < 0.01$, Mann-Whitney U test). (**G**) Schematic illustrating the part of retinal tissue where images in (H) and (J) were obtained, namely, the glial lamina. (**H**) GFAP signal in the ONH of 3-mo Glia-KO mice was stronger than that of Ctr mice. (**I**) *Gfap* mRNA levels were also significantly higher in 3-mo Glia-KO mice (n = 3, $^{**}P < 0.01$, Mann-Whitney U test). (**J** and **K**) At 12 mo, both GFAP protein and *Gfap* mRNA levels in Glia-KO mice were lower than those in Ctr mice (n = 3, $^{**}P < 0.01$, Mann-Whitney U test).

glutamate uptake by astrocytes. To examine whether RGCs in Glia-KO mice were more susceptible to excitotoxic damage, we injected a relatively low dose of NMDA into the eye (0.2 nmol per eye) (Fig. 7, L and M). Ctr mice (12 months) showed a 14.1% reduction in Rbpms$^+$ RGCs, whereas Glia-KO mice (12 months) exhibited a 36.5% reduction in RGCs. These results demonstrate that ABCA1 deficiency induced inflammation in astrocytes, which probably exacerbated excitotoxicity within a specific RGC subtype.

DISCUSSION

Our data demonstrate that astrocyte dysfunction by *Abca1* deficiency triggered optic neuropathy–like phenotypes in mice without affecting IOP. Although the rodent retina lacks some anatomical structures seen in humans, including a macula and extracellular matrix plate of lamina cribrosa, Glia-KO mice showed several anatomical features potentially relevant to NTG: age-associated RGC degeneration, swelling and loss of the ON, thinning of inner retinal layers, synapse loss, and reduction in ocular responses. It is still unclear whether the SNPs found in human glaucoma patients reduce ABCA1 function, but some mouse glaucoma models show 15 to 50% reduction in retinal *Abca1* (*33*, *49*). A previous study showed that overexpression of human *ABCA1* protected RGCs against experimental glaucoma in mice (*50*). These reports strongly suggest that the loss of ABCA1 is linked to RGC damage. The present study revealed that loss of function of ABCA1 rather than gain of toxic function, especially in astrocytes, was important for triggering age-associated optic neuropathy.

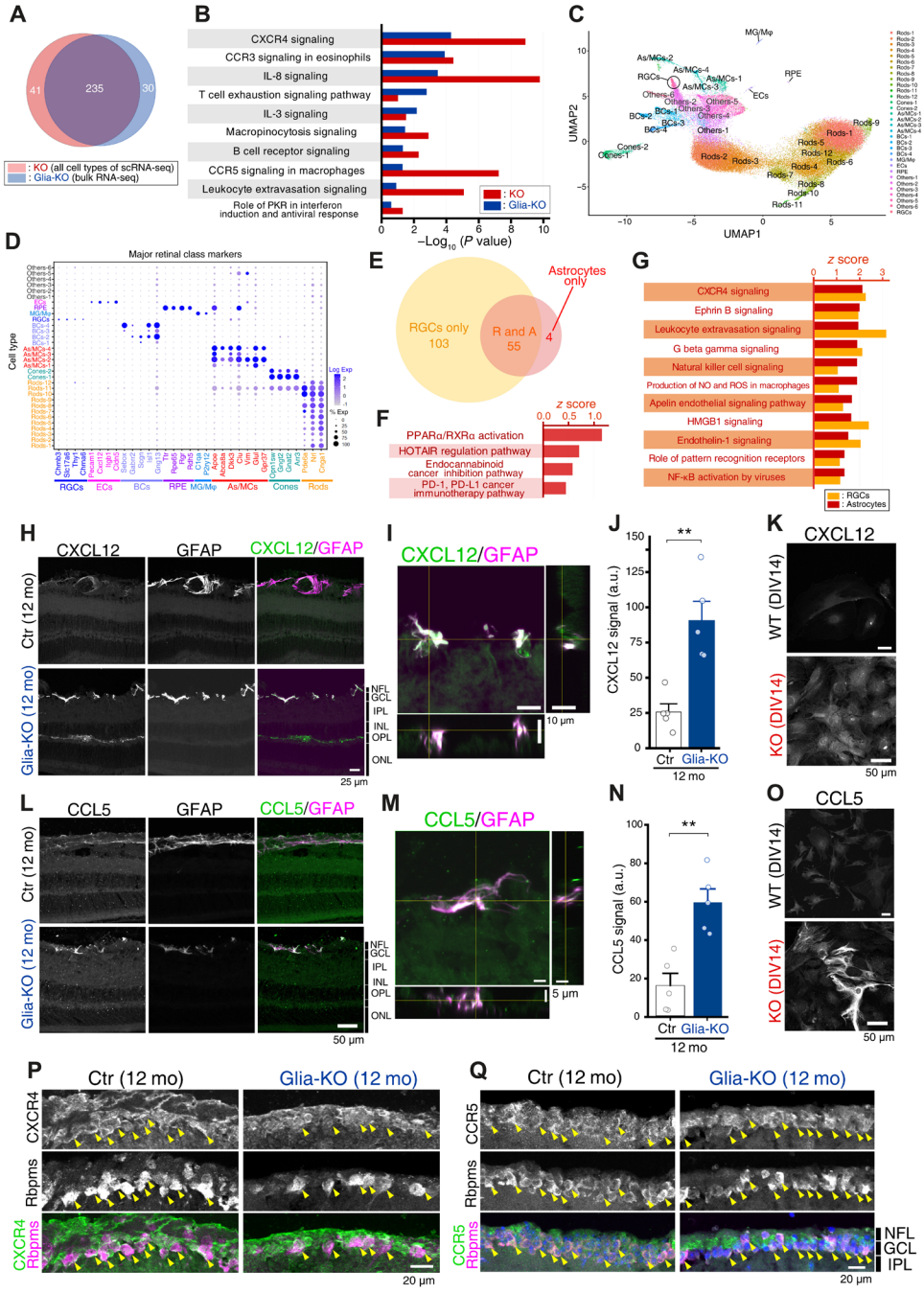

Fig. 6. Bulk and scRNA-seq analysis of retinae. (**A**) Comparison of up-regulated pathways in all retinal cell types of KO and Glia-KO mice at 12 mo. Most up-regulated pathways were shared between KO and Glia-KO mice. (**B**) Ingenuity Pathway Analysis identified that the inflammatory pathway was one of the most common disease-related pathways between KO and Glia-KO mice, including cytokine/chemokine signaling and immune cell responses. (**C**) Uniform Manifold Approximation and Projection visualization of the transcriptional heterogeneity of 62,479 retinal cells from 12-mo WT and KO mice. Clusters are colored according to cell type. (**D**) Dot plot showing gene combinations (column) uniquely indicating cell clusters (row). (**E**) Venn diagram of up-regulated pathways in KO mice. (**F** and **G**) Pathways up-regulated (F) selectively in astrocytes and (G) in both RGCs and astrocytes. (**H** to **J**) CXCL12 was up-regulated in astrocytes of 12-mo Glia-KO mice. (I) CXCL12 signals colocalized with GFAP signals in Glia-KO mice. (J) The signal intensity of CXCL12 was increased by approximately 3.5-fold in astrocytes ($n = 5$ eyes, $^{**}P < 0.01$, Mann-Whitney U test). (**K**) CXCL12 was also up-regulated in cultured ON KO astrocytes. (**L** to **N**) CCL5 signals colocalized with GFAP signals in both 12-mo Ctr and Glia-KO mice. (N) The signal intensity of CCL5 in astrocytes was threefold higher in Glia-KO mice ($n = 5$ eyes, $^{**}P < 0.01$, Mann-Whitney U test). (**O**) CCL5 was also up-regulated in cultured ON KO astrocytes. (**P** and **Q**) CXCR4 and CCR5 were expressed in Rbpms$^+$ RGCs regardless of genotype (i.e., Ctr or Glia-KO). Data represent means ± SEM.

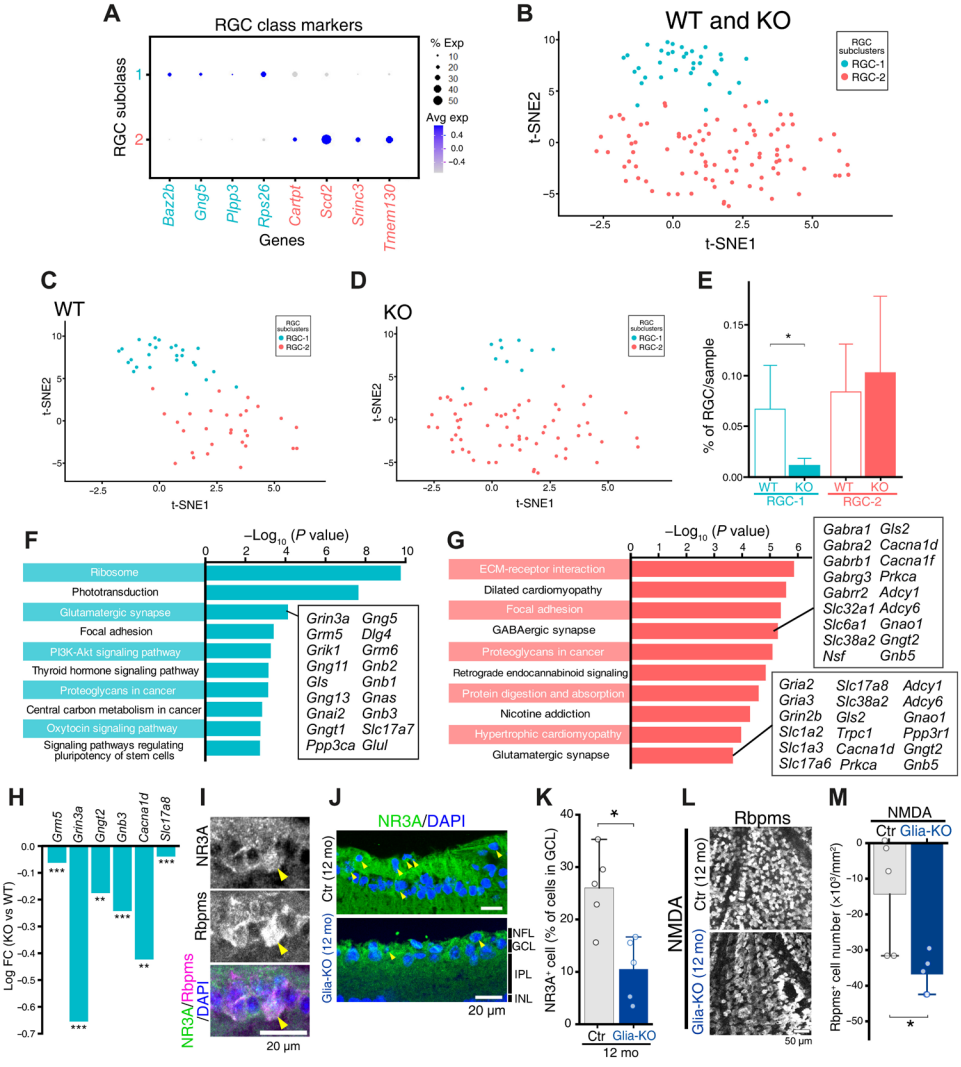

Fig. 7. Identification of a novel RGC type sensitive to ABCA1 deficiency in astrocytes. (**A**) Dot plot showing RGC subclasses (columns) and marker genes (rows). (**B**) Subclustering of RGC populations visualized by t-distributed stochastic neighbor embedding. (**C** and **D**) The number of dots indicating RGC-1 was reduced in 12-mo (D) KO mice compared with (C) WT mice. (**E**) Percentages of RGC-1 per sample were significantly reduced in KO mice compared with those in WT mice. In contrast, RGC-2 numbers were not reduced ($n = 3$ and 5 for WT and KO, respectively; $^*P < 0.01$, Mann-Whitney U test). (**F** and **G**) Kyoto Encyclopedia of Genes and Genomes pathways with (F) enrichment or (G) reduced enrichment in RGC-1. RGC-1 showed enrichment of genes associated with the glutamatergic synapse pathway and reduced enrichment of GABAergic synapse pathway gene expression. *Grin3a* was enriched in RGC-1, while other genes were enriched in RGC-2. (**H**) RGC-1 glutamatergic synapse genes were significantly down-regulated in 12-mo KO mice. *Grin3a* exhibited the greatest reduction ($n = 16$ and 5 cells for WT and KO, respectively; $^{**}P < 0.01$ and $^{***}P < 0.001$, Wilcoxon rank sum test). (**I** to **K**) NR3A was (I) expressed in Rbpms$^+$ RGCs and (J) down-regulated in 12-mo Glia-KO compared with Ctr mice. (K) Numbers of NR3A-expressing cells were significantly reduced in 12-mo Glia-KO mice. (**L** and **M**) Glia-KO RGCs exhibited higher sensitivity to excitotoxicity. Low-dose NMDA (0.2 nmol per eye) caused ~15% reduction in RGC numbers in 12-mo Ctr mice that was exacerbated in Glia-KO mice ($n = 5$ retinae, $^*P < 0.05$, Mann-Whitney U test).

We identified that the cell type highly expressing ABCA1 in the retina was astrocytes, in addition to lower expression levels in previously reported cell types, such as retinal pigment epithelium, monocyte-lineage cells, and photoreceptors. Although the scRNA-seq database provided by the Human Protein Atlas Project also shows enrichment of *ABCA1* mRNA in cone photoreceptors (cone cells) and BCs of the human retina (*51*), it does not contain a retinal astrocyte population. Another human database also indicated that cone cells and BCs are the cell types most enriched for *ABCA1* expression, whereas astrocytes come in third (*52*). One possible explanation is differences in ABCA1 protein stability between cell types. For example, oxysterol-binding protein (OSBP) negatively regulates ABCA1 protein stability (*53*). *OSBP2* expression in cone cells and BCs was 6.7- and 17.7-fold higher than observed in astrocytes of the human retina (*52*). In addition, expression of OSBP-related protein 8, another negative regulator of ABCA1 expression (*54*), was five-fold higher in these cell types compared with astrocytes (*52*). Conditional deletion of *Abca1* in cone photoreceptors did not elicit neurodegeneration (*55*), indicating that these cell types have only a minor role (if any) in ABCA1-mediated RGC damage. Human Müller cells and RGCs also express *ABCA1* mRNA at only minor levels (*52*), consistent with our results. In addition, ABCA1 protein in the human retina was observed to occur in a fibrous pattern in the innermost layer of the retina and did not overlap with the 4′,6-diamidino-2-phenylindole

(DAPI) signal of the GCL, which is presumed to indicate RGCs (*3*). Another human study also reported strong expression of ABCA1 in the glial tube of the ON (*4*), suggesting that astrocytes but not RGCs may express ABCA1 in human ocular tissue. Because astrocytes tightly enwrap RGC axons, astrocytic dysfunction would directly cause axonal impairment and RGC damage. In agreement with this expectation, Glia-KO mice exhibited apoptosis of RGCs but not other retinal neurons. We also found that ABCA1 protein and mRNA were highly enriched in the ONH and ON, where no cone cells, BCs, or Müller cells are present. On the basis of these previous studies and our data, we concluded that ABCA1 is enriched in astrocytes. To our knowledge, this is the first report to demonstrate that ABCA1 is highly expressed in ocular astrocytes.

Our results show ON loss and RGC death in Glia-KO mice. Similarly, topographic loss of RGC soma and the ON has been reported in human glaucoma (*38*, *56*). We did not investigate topographic RGC soma loss in the present study, but it will be estimated in a future study. Instead, we observed regional ON loss in horizontal ON sections, as well as regional impairment of ocular function in mfERG. The results suggest that Glia-KO mice have topological damage of RGCs. In the ONH, Glia-KO mice exhibited loss of axonal markers at the posterior part of the glial lamina, consistent with previous reports of animal glaucoma models (*36*, *37*) and patients (*28*). Such similarities in tissue damage suggest that Glia-KO mice exhibit phenotypes potentially relevant to glaucoma.

RGC degeneration was not observed at a young age, although astrocytes had already become hypertrophic. Because astrocytes are important in the initiation and/or progression of neurodegenerative diseases (*57*, *58*), and the overinduction of astrocyte reactivity accelerates neuronal death (*15*), the hypertrophic astrocytes in 3-mo Glia-KO mice may reflect the initiation of the disease. RGC damage may require long-term accumulation of astrocyte abnormalities. At 3 months, KO astrocytes may already be neurotoxic, but the protective nature of surrounding cells and resistance of RGCs to astrocyte dysfunction prevents RGC loss. In such cases, the loss of protective mechanisms and resilience associated with aging may trigger injury of RGCs. Another possibility is that young KO astrocytes are less injurious and become more neurotoxic with age. Supporting this hypothesis, KO astrocytes showed different hypertrophies at 3 and 12 months. Because aged KO astrocytes exhibited significantly up-regulated chemokine expression, inflammation may contribute to age-associated increases in astrocytic neurotoxicity. In addition, aged KO astrocytes were less hypertrophic. Loss of astrocyte hypertrophy exacerbates ocular hypertension–induced RGC loss (*59*). Following brain injury, hypertrophic astrocytes are important for limiting inflammation and protecting neurons (*14*). Accordingly, reductions in astrocyte hypertrophy may be linked to their loss of neuroprotective and anti-inflammatory functions. In combination with a loss of protective functions and gain of neurotoxicity in astrocytes, RGCs and other cell types may trigger RGC degeneration.

In the present study, the rate of RGC loss was relatively small, which was similar to Amyloid precursor protein (APP) gene with Swedish mutation and presenilin 1 gene (PS1) with deletion of exon 9 mice (*15*) in that both models show severe pathological phenotypes and altered astrocyte hypertrophy. Glia-KO mice already showed hypertrophic retinal astrocytes at 3 months, which was followed by RGC loss, suggesting that the phenotypic changes of retinal astrocytes are important for the initiation of non–cell-autonomous RGC death and induction of a glaucoma-like phenotype. In the APP/PS1 mouse model of Alzheimer's disease, the severity of astrogliosis is well associated with that of disease-like symptoms (*15*). For this, astrocytic MAOB–mediated H_2O_2 has a critical role. In Huntington's disease (HD) model, overexpression of mutant huntingtin genes in astrocytes triggers HD-like pathology (*57*). Mutant huntingtin decreased astrocytic glutamate transporter and caused excitotoxicity in adjacent neurons, thereby leading to an HD phenotype. In an amyotrophic lateral sclerosis (ALS) model, astrocytes with mutant SOD1 increased progression of ALS by activating microglial inducible nitric oxide synthase (*58*). Therefore, although the method of astrocytic contribution varies from disease to disease, non–cell-autonomous mechanisms exerted by astrocytes appear to be common in many CNS diseases, which would also be the case in the present study.

ABCA1 deficiency–triggered inflammatory responses by astrocytes may be mediated in part by the accumulation of cholesterol, a major substrate of ABCA1. A previous study demonstrated that cholesterol accumulation enhances Toll-like receptor (TLR)–mediated inflammatory signaling (*60*). Because TLR localizes at cholesterol-rich lipid microdomains (also called lipid rafts) in the plasma membrane, excess cholesterol exacerbates TLR-mediated signaling. Consistent with this notion, our RNA-seq data showed up-regulation of PRR and NF-κB pathways, two major downstream targets of TLR signaling. ABCA1 deficiency in astrocytes may also cause an inadequate cholesterol supply to neurons. Impairments of astrocyte-to-neuron cholesterol supply trigger neurodegenerative diseases (*61*), and a lack of neuronal cholesterol mediates excitotoxic neuronal death (*62*). Because astrocyte-derived cholesterol may be required for synaptogenesis of RGCs (*63*), ABCA1 deficiency in astrocytes may also trigger synapse loss in RGCs. Consistent with this notion, Glia-KO mice showed reduced numbers of synapses in the IPL. Collectively, previous reports and our results suggest that ABCA1 deficiency–induced inflammation, synapse loss, and RGC degeneration may be mediated in part by cholesterol.

Accumulating evidence suggests that inflammation is a key process in the pathogenesis of glaucoma. Elevated inflammatory signals can be detected in the retina of patients with glaucoma (*64*). Astrocytes play a central role in inflammation of the human glaucomatous eye (*64*). Our scRNA-seq analysis revealed up-regulation of inflammatory pathways (e.g., HMGB1, PRRs, and NF-κB) and chemokine pathways (e.g., CXCR4, CCR3, and CCR5) in astrocytes and RGCs. Moreover, *Abca1*-deficient astrocytes expressed higher levels of CXCL12 and CCL5, agonists for these receptors. Both CCL5 and CXCL12 are expressed in the ocular tissue of patients with glaucoma (*65*, *66*). Because our results and human scRNA-seq data (*52*) showed expression of CXCR4 and CCR5 in RGCs, astrocyte-derived chemokines likely target RGCs. Although CXCL12 also exhibits a neuroprotective effect, CXCL12 truncated by matrix metalloproteinase is highly neurotoxic (*67*). Notably, because matrix metalloproteinase is often associated with inflammation, such chemokine signals may be converted into neurotoxic signals. ABCA1 deficiency can also reduce anti-inflammatory responses by down-regulating JAK2/STAT3 (Janus kinase 2/signal transducer and activator of transcription 3) signaling (*68*).

Although previous scRNA-seq analyses have revealed the heterogeneity of RGCs (*30*), including differences in resiliency or sensitivity to ON crush (ONC) (*31*), it was unknown whether any particular RGC subtype is sensitive to glaucoma, especially NTG. We identified a novel RGC subclass that is sensitive to *Abca1* deletion and highly expresses *Grin3a* (which encodes NR3A). NR3A functions as a "dominant-negative"–like subunit in NMDA receptors to reduce

Ca^{2+} permeability (*46*). Loss of *Grin3a* in RGC-1 cells would cause Ca^{2+} excitotoxicity (*46*, *48*), a common neurodegenerative mechanism in various neurologic disorders. The finding that dysregulated *GRIN3A*/NR3A is linked to human neurodegenerative diseases (*69*) further supports our DFA results. In addition, our results showed a reduction in GABAergic signaling in RGC-1. In addition to the cell-autonomous mechanism, we observed a reduction of the putrescine degradation/MAOB-mediated GABA production pathway, which is important for astrocyte-mediated tonic inhibition (*15*). Thus, it is possible that the reduced inhibition provided by astrocytes enhances the excitotoxicity of RGCs. Furthermore, because cultured KO astrocytes showed a significant increase in extracellular glutamate levels, ABCA1 loss may enhance glutamate release or reduce uptake by astrocytes. Disruption of the balance between inhibitory and excitatory signaling by astrocytes may also mediate the non–cell-autonomous mechanism of RGC excitotoxic damage, thus contributing to retinopathy in Glia-KO mice. Previous scRNA-seq studies revealed 45 subclasses of RGCs (*30*, *31*), of which *Grin3a* was expressed in 16 subclasses occupying ~25% of the total RGC population [as calculated using Subtype Gene Browser (*30*, *31*)]. Four RGC subclasses expressed *Grin3a* under control conditions but exhibited significantly reduced expression after ONC: C4, C28, C31, and C43. These RGC subclasses included α-RGCs, F-RGCs, and ipRGCs. Among these classes, only F-RGC [a direction-selective RGC (*70*)] was sensitive to both ONC and ocular hypertension (*31*, *71*). Consistent with the vulnerability of direction-selective RGCs in mouse glaucoma models, motion sensitivity was impaired before visual field loss in patients with glaucoma (*72*). On the basis of these reports, the most probable candidate for RGC-1 seems to be direction-selective RGCs.

Many studies, including non–human primate glaucoma models, have demonstrated excitotoxicity in RGCs (*73*). Our results identify a possible link between chemokine signaling and excitotoxicity in RGCs. CXCR4 and CCR5 are known to mediate neuronal death (*74*). CCL5 facilitates glutamate release from neurons (*75*), while CXCL12 is coupled to glutamatergic signaling and NMDAR-mediated neurotoxicity (*76*). Furthermore, reductions in neuronal cholesterol mediate excitotoxicity (*62*). Collectively, these reports suggest that an association between astrocyte-derived chemokines and reduced cholesterol supply enhances excitotoxicity in RGCs. The finding that RGCs of Glia-KO mice showed higher vulnerability to excitotoxicity supports this possibility. However, it is difficult to protect RGCs by solely inhibiting glutamatergic signaling in patients (*77*) because glaucoma is a multifactorial disease, and other factors, such as oxidative stress, may contribute to RGC death. We also observed up-regulation of oxidative stress pathways in RGCs of KO mice, suggesting that excess excitatory signaling was accompanied by other pathological changes that cause RGC degeneration, such as oxidative stress. Accordingly, inhibition of multiple targets may be necessary for glaucoma treatment. As summarized in Fig. 8, our results demonstrate that *Abca1* deficiency, especially in astrocytes, causes age-associated optic neuropathy–like phenotypes without IOP changes. Astrocytic ABCA1 may be an important pathogenic factor in optic neuropathy and a potential molecular target for the treatment of glaucoma, especially NTG.

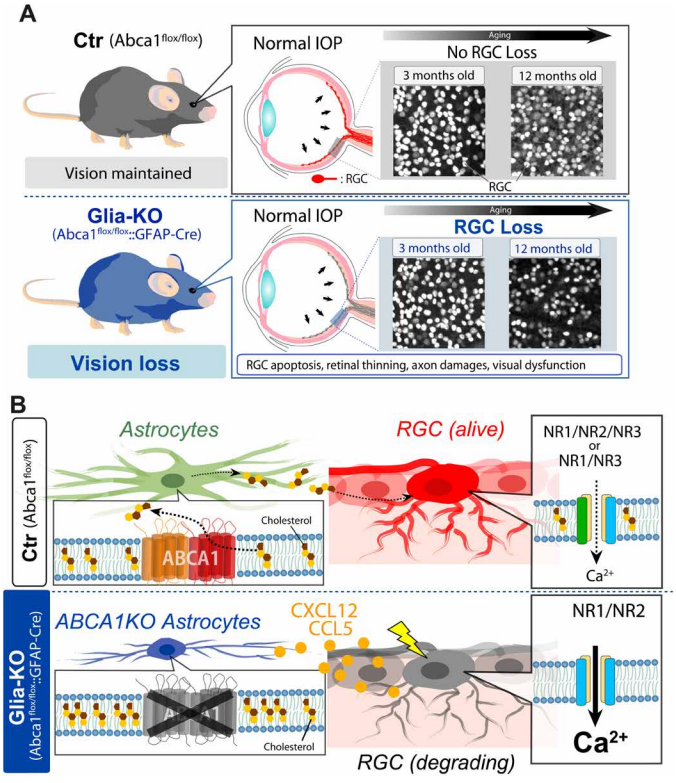

Fig. 8. Astrocytic ABCA1–triggered pathogenesis of optic neuropathy. In summary, loss of astrocytic ABCA1 caused optic neuropathy–like phenotypes. (**A**) Glia-KO mice showed age-associated optic neuropathy–like phenotypes such as RGC degeneration, retinal thinning, axonal damage, and visual dysfunction without IOP changes. (**B**) At the cellular level, ABCA1-deficient astrocytes showed impaired efflux and intracellular accumulation of cholesterol. Aged astrocytes reduced their hypertrophy and triggered inflammation by producing chemokines such as CXCL12 and CCL5, which would target CXCR4 and CCR5 expressed on RGCs. A subclass of RGCs (i.e., RGC-1) was sensitive to *Abca1* deletion. RGC-1 expressed high levels of the NR3A subunit gene (*Grin3a*), which reduces Ca^{2+} permeability of the NMDA receptor channel. In Glia-KO mice, RGC-1 reduced *Grin3a* expression, and RGCs exhibited higher sensitivity to NMDA-evoked excitotoxicity. Thus, astrocyte-derived chemokines may enhance NMDA receptor–mediated excitotoxicity of RGC-1.

MATERIALS AND METHODS

Materials used in the present study are listed in table S1. No statistical methods were used to predetermine the sample size. Experiments were not randomized. The investigators were blinded to group allocations during experiments and when counting numbers of RGCs and apoptotic cells to assess outcomes.

Animals

A list of mouse strains used in the study is presented in table S1. Mice were maintained in a pathogen-free, temperature-controlled (23°C), and humidity-controlled (55%) facility with a 12-hour (6:00 a.m. to 6:00 p.m.) light-dark cycle. Mice had free access to food and water. WT male mice (DBA/1J) were obtained from Japan SLC (Shizuoka, Japan). KO (DBA/1J background) and Glia-KO ($ABCA1^{flox/flox}$::GFAP-Cre, C57BL/6J background) mice were provided by F. Okajima (Gunma University, Japan) and M. Hayden (British Columbia, Canada), respectively. As a control (Ctr) for Glia-KO mice, we used littermate $ABCA1^{flox/flox}$ mice. All animal experiments were replicated at least three times.

IOP measurement

IOP was measured using a rebound-type tonometer (TonoLab, Icare, Vantaa, Finland) as previously reported (*33*). Mice were anesthetized

with a mixture of medetomidine [0.3 mg/kg body weight (b.w.)], midazolam (4.0 mg/kg b.w.), and butorphanol (5.0 mg/kg b.w.). IOP was measured after loss of the righting reflex. All IOP measurements were performed between 6:00 p.m. and 12:00 a.m.

Central corneal thickness

Measurement of CCT was performed as previously reported (*33*). Briefly, enucleated eyes were fixed with 4% paraformaldehyde (PFA) for 1 hour at room temperature, and corneas were dissected. Cell nuclei were labeled with DAPI (10 μg/ml in phosphate-buffered saline, PBS) for 1 hour in the dark at room temperature. Corneas were imaged by z-stack imaging using an FV-1200 laser-scanning confocal microscope (Olympus, Tokyo, Japan).

Spectral-domain optical coherence tomography

Spectral-domain optical coherence tomography (OCT) (RS-3000, Nidek, Aichi, Japan) was used to measure retinal thickness. Briefly, a 60-D adapter lens was placed on the objective of the multiline OCT instrument. Retinal scanning was performed vertically through the center of the ONH at a three-disc-diameter length above the ONH. The thickness of the ganglion cell complex was measured from the internal limiting membrane to the IPL and INL interface. The maximum number of B scans set by the manufacturer (50 for line scans) was used for averaging.

Preparation of flat-mount retinae

Eyes were enucleated, immersed in 4% PFA for 30 min at room temperature, and then dissected. Retinae were post-fixed overnight at 4°C and divided into quadrants for subsequent experiments. A specific retinal area was not used (i.e., nasal, temporal, ventral, or dorsal). Each quadrant retina was used as one flat-mount retinal sample for immunohistochemistry. Images used for quantification of numbers of RGCs and apoptotic cells were obtained from the central retina (~500 μm from the ONH).

Preparation of tissue sections

For immunofluorescence staining of ABCA1, enucleated eyes were immediately immersed in Tissue-Tek Optimal Cutting Temperature (O.C.T.) compound (Sakura Fintechnical, Tokyo, Japan) and frozen at −80°C. Eye sections (20-μm thickness) were prepared using a cryostat (LC1520, Leica, Wetzlar, Germany) and mounted on glass slides. Tissues on the slides were fixed in 4% PFA for 5 to 10 min at room temperature. To investigate other proteins, enucleated eyes were immersed in 4% PFA overnight at 4°C, soaked in 20% sucrose/PBS for 2 days at 4°C, and cut into 20-μm sections. For ONH, globes with attached ONs were isolated and fixed in 4% PFA overnight at 4°C. ONs were dissected 0.5 to 1.0 mm posterior to the sclera, and tissues were immersed in 20% sucrose/PBS for 2 days at 4°C. Samples were then cryoprotected and sliced (10-μm thickness).

Magnetic cell separation

Tissue dissociation and separation of cell types were performed with a gentleMACS Dissociator and Adult Brain Dissociation Kit according to the manufacturer's protocol (Miltenyi Biotec, Bergisch Gladbach, Germany). Three retinae per sample were dissociated. Briefly, retinae were minced and digested with a proprietary enzyme solution. Next, samples were mixed with Fc receptor blocking reagent and incubated with anti-mouse CD11b–coated microbeads for 10 min at 4°C. $CD11b^+$ microglial cells were collected using an LS column on a QuadroMACS Separator (Miltenyi Biotec). To further separate astrocytes/Müller cells and other cell types (i.e., neurons and endothelial cells), the flow-through was mixed with anti–ACSA-1–coated microbeads for 10 min at 4°C, and the astrocyte/Müller cell fraction was magnetically trapped on the LS column. The flow-through after removing $CD11b^+$ and $ACSA\text{-}1^+$ cells was used as the negative fraction.

RNA purification and reverse transcription

Total RNA from ocular tissues or isolated cells was purified using an RNeasy lipid tissue mini kit (Qiagen, Hilden, Germany) according to the manufacturer's instructions. Tissues or cells were homogenized in QIAzol for 40 s and mixed with chloroform, and the resulting water phase was transferred to a new tube. EtOH (70%) was added, and RNAs were bound to the spin column. After washing and eluting RNAs, reverse transcription was performed using a PrimeScript RT reagent kit (Takara Bio, Shiga, Japan) according to the manufacturer's protocol.

Bulk RNA-seq

Isolated retinae from Glia-KO mice were lysed, and total RNA was isolated using an RNeasy Lipid Tissue Kit (Qiagen). Samples were assessed using an RNA 6000 Nano Kit (Agilent, Santa Clara, CA, USA) and 2100 Bioanalyzer (Agilent). Total RNA samples >200 ng with an RNA integrity number >8.0 were sequenced. The sequencing library was prepared using a TruSeq Stranded mRNA Library Prep Kit (Illumina, San Diego, CA, USA). Poly-A RNA was purified using poly-T oligo–attached magnetic beads. The eluted mRNA was subsequently fragmented by incubation with first-strand buffer at 94°C for 8 min. First-strand cDNA was synthesized by incubating a mixture of cleaved RNA fragments, Superscript II reverse transcriptase, and random primers in a thermal cycler (25°C for 10 min, 42°C for 15 min, and 70°C for 15 min; hold at 4°C). cDNA was labeled using a cDNA plate barcode label reagent. Samples were then mixed with DNA polymerase I, ribonuclease H, and barcode label reagents, and incubated at 16°C for 10 min to synthesize second-strand cDNA and digest the template RNA. cDNA was purified with AMPure XP beads, the 3′ ends were adenylated using an A-tailing mix, and the mixture was incubated in a thermal cycler (37°C for 30 min and 70°C for 5 min; hold at 4°C). Adapters were ligated to cDNA using a ligation mix, and the mixture was incubated at 20°C for 15 min. After several rounds of polymerase chain reaction (PCR) amplification, enriched DNA fragments were purified with AMPure XP beads. The quality and quantity of the library were then validated with an Agilent 2100 Bioanalyzer. Bulk RNA-seq was performed with an Illumina NovaSeq 6000 according to the manufacturer's procedures, and approximately 6.36 Gb were read per sample. Reads mapped to ribosomal RNA and those with low-quality, adaptor pollution, or a high content of unknown bases were removed using SOAPnuke to produce clean reads, which were stored in FASTQ format for subsequent analyses. RNA-seq files were analyzed using Galaxy Tools (usegalaxy.org). Paired-end FASTQ files were aligned to the GRCm38 mouse genome using HISAT2 (v2.1.0), and BAM files were created. Aligned reads were then counted using featureCounts (v1.6.4) to create gene count tables, which were analyzed by DESeq2 (v1.22.1) to identify differentially expressed genes. Log-fold change and *P* value per gene were then used to perform ontological analysis via IPA.

Single-cell RNA sequencing

WT and KO mice at 12 months of age were euthanized with a CO_2 chamber. Their eyes were dissected and placed on a glass slide with

a shallow volume of PBS. While using angled forceps to hold the eye in position, small spring scissors were used to create an incision at the cornea-sclera junction. The scissors were then used to cut along the divide around the eye until the cornea and iris were lifted, and the lens was released. The retina was then gently removed from the eyecup using angled forceps and carefully separated from the choroid layer. After obtaining retinal tissue from mouse eye dissection, a Papain Dissociation System (Worthington, Columbus, OH, USA) was used to dissociate tissues into a single-cell suspension. The conditions were initially tested using a C1 machine (Fluidigm, South San Francisco, CA, USA) and confirmed with a 10X Chromium system (10X Genomics, Pleasanton, CA, USA). Briefly, the retinal tissue was placed in a mixture of 100 μl of papain solution and 5 μl of deoxyribonuclease solution and then incubated at 37°C for 15 min after gentle titration. The dissociated cell solution was then diluted with 900 μl of PBS and passed through a 35-μm cell filter. Dissociated samples were loaded onto the 10X Chromium system, and scRNA-seq libraries were prepared using a Chromium Single-Cell 3′ reagent kit (v3). According to the manufacturer's protocol, single cells were captured in nanoliter-scale Gel Beads-In-Emulsion (10X Genomics), whereby cells were lysed, cDNA was synthesized by reverse transcription of RNA, and all cells were tagged with the same 10X barcode. Following PCR amplification, enzymatic fragmentation, adaptor attachment, and sample indexing, the constructed library was sequenced with the NextSeq 500 system (Illumina).

Bioinformatic and computational analysis

Demultiplexing NextSeq sequencer base call files were used to generate FASTQ files of sequencing reads using the 10X Genomics Cell Ranger command mkfastq (version 3.0.2). Feature count matrices were then generated using the Cell Ranger command count, which performs read alignment to the GRCm38 mouse genome and unique molecular identifier counting. Because the default Cell Ranger cell detection algorithm for generic cell types is too restrictive when applied to low-expressing retinal cells, we used the -forcecells 9000 parameters to extract a higher number of cell barcodes per tissue sample. This assumes that 9000 cells were captured per sample and loaded onto the 10X Chromium system, which aligns with the usual uptake percentage of cell suspension loaded given the fixed density and volume suggested by technicians at the Queen Mary University of London Genome Center. The R toolkit package Seurat (v3.1.4; https://github.com/satijalab/seurat) was used for further downstream analysis. Cell barcodes, genes, and expression count matrices of each sample were separately loaded into Seurat with a prefilter of a minimum of 200 genes detected per sample. Log normalization, which normalizes the feature expression for each cell within the sample, and feature selection, which extracts genes exhibiting high cell-cell variation within the dataset, were performed for each sample dataset. Following normalization, all sample datasets were integrated using FindIntegrationAnchors and IntegrateData, which use an anchoring method to coordinate cell types among different samples and integrate them into one Seurat object dataset. The integrated dataset was then scaled, and principal components analysis was performed. The top 20 principal components were used for a graph-based clustering approach. In brief, the clustering steps involved construction of a K-nearest neighbor graph, refinement of edges using Jaccard similarity, and optimization with the Louvain algorithm with a granularity setting of 1.5. The resulting 32 clusters were then projected to a two-dimensional plane and visualized as a Uniform Manifold Approximation and Projection. The FindAllMarkers function was then applied to extract differentially expressed genes per cluster by comparing each cluster with the remaining dataset using the Wilcoxon rank sum test. Known retinal cell markers were then identified in these differential gene lists to assign cell identities to the respective clusters. Numbers of cells that expressed two of four marker genes (*Slc17a6*, *Stmn2*, *Thy1*, and *Resp18*) were used to estimate changes in numbers of RGCs between WT and KO mice.

Real-time PCR

The reaction mix contained total RNA, primers, probes, and PrimeTime Gene Expression Master Mix. PCR amplification and real-time detection were performed using an Applied Biosystems 7500 Real-Time PCR System (Waltham, MA, USA). The temperature profile consisted of 95°C for 3 min, followed by 40 cycles of denaturation at 95°C for 15 s and annealing/extension at 60°C for 1 min. Predesigned primers and probes for the investigated genes (listed in table S1) were obtained from Integrated DNA Technologies (Coralville, IA, USA).

Immunofluorescence staining

Flat-mount retina samples were blocked with 5% normal goat serum in PBS containing 2% Triton X-100 (PBST) for 1 hour at room temperature. For ABCA1 immunostaining, samples were further blocked using an Mouse on Mouse (M.O.M.) Kit (Vector Labs, Burlingame, CA, USA) according to the manufacturer's protocol. Retinal slices or flat-mount retinae were incubated with primary antibodies overnight or for 3 days at 4°C, respectively. Samples were washed three times with PBST at room temperature for 10 min each and incubated with Alexa-conjugated secondary antibodies for 1 hour at room temperature. Primary and secondary antibodies were diluted in blocking buffer and PBST containing 0.3% normal goat serum, respectively. Nuclei were stained with DAPI. For filipin III staining, samples were incubated in filipin III solution (50 μg/ml in PBS) for 1 hour at room temperature. Samples were mounted on glass coverslips using ProLong Gold (Thermo Fisher Scientific, Waltham, MA, USA). Fluorescent images were acquired using an FV1200 laser scanning confocal microscope (Olympus). A normal adult human retina (female, 42 years old, T1234108; BioChain Institute, Newark, CA, USA) was used for ABCA1 immunostaining.

In situ hybridization

In situ hybridization was performed as previously reported (*33*). An antisense riboprobe was used to detect *Abca1* [GenBank accession number NM_013454, full length, 1 to 6786 nucleotides (nt)]. Digoxigenin (DIG)–labeled riboprobes were synthesized from each plasmid using in vitro transcription (DIG RNA Labeling Mix, Roche). Cryosections were fixed in 4% PFA and treated with Proteinase K (1 μg ml^{-1}; Merck) for 10 min. Samples were further fixed in 4% PFA, acetylated, and then hybridized with DIG-labeled probes in hybridization buffer [50% formamide, 5× saline sodium citrate (SSC) (1× SSC: 0.15 M NaCl, 0.015 M sodium citrate in diethylpyrocarbonate-treated water), yeast transfer RNA (200 μg ml^{-1}), heparin (0.1 mg ml^{-1}), 1× Denhardt's solution, 0.2% Tween 20, 0.1% CHAPS, and 5 mM EDTA] overnight at 65°C. Hybridized sections were washed with 1× SSC containing 50% formamide at 65°C for 15 min (wash I) and 30 min (wash II) and with 0.1× SSC at 65°C for 30 min (wash III). Then, the sections were washed twice with maleic acid buffer [0.1 M maleic acid (pH 7.5), 0.1% Tween 20, and 0.15 M NaCl] and incubated with alkaline phosphatase–conjugated anti-DIG antibody

(1:2000; Roche, Basel, Switzerland) in blocking buffer (0.5% skim milk in PBS) overnight at 4°C. Alkaline phosphatase was visualized by staining with nitro-blue tetrazolium chloride (Roche) and 5-bromo-4-chloro-3-indolyl-phosphate (Roche) according to the manufacturer's instructions. For double staining, immunohistochemistry was performed following in situ hybridization. Transmitted light images were obtained with an Olympus BX53 microscope connected to a charge-coupled device camera (DP72; Olympus) or a BZ-X700 microscope (KEYENCE, Tokyo, Japan).

Multifocal electroretinograms

mfERGs were recorded using a VERIS 6.0 system (Electro-Diagnostic Imaging, Redwood City, CA, USA) as previously reported (*39*). Mice were anesthetized, and their pupils were dilated with 0.5% phenylephrine hydrochloride and 0.5% tropicamide. The visual stimulus consisted of seven hexagonal areas scaled for eccentricity. The stimulus array was displayed on a high-resolution black-and-white monitor at a frame rate of 100 Hz. The second-order kernel was previously shown to be a sensitive indicator of inner retinal dysfunction (*42*) and impaired in patients with glaucoma (*43*). We analyzed the second-order kernel amplitude of mice.

Serial block-face scanning electron microscopy

Enucleated eyes were immersed in 0.1 M PBS containing 4% PFA (Fujifilm Wako Pure Chemical Corporation, Osaka, Japan) and 0.5% glutaraldehyde (Fujifilm Wako Pure Chemical Corporation) for 12 hours at 4°C. ON sections were cut on a vibratome (Leica), and the resulting specimens were stained with 0.4% OsO_4, uranyl acetate, and lead aspartate, followed by embedding in epon resin (Electronic Microscopy Sciences, Hatfield, PA, USA). SBF-SEM images were obtained with a Sigma VP scanning electron microscope (Carl Zeiss, Oberkochen, Germany). Axonal swelling was defined as axonal segments with a diameter greater than twice that of adjacent segments, with prominent accumulation of membranous organelles and a lack of continuous cytoskeletal bundle profiles.

Measurement of total cholesterol

Total cholesterol was measured using a LabAssay cholesterol kit according to the manufacturer's protocol (Fujifilm Wako Pure Chemical, Tokyo, Japan). Briefly, chromogen reagent was mixed with reaction buffer to generate a working solution. An aliquot of each sample (2 μl) was used for cholesterol measurement. The reaction mixture was incubated at 37°C for 5 min, and the absorbance of samples was measured with a microplate reader at 600 nm (SpectraMax 340PC384, Molecular Devices, San Jose, CA, USA).

Intravitreal NMDA injection

To investigate excitotoxic RGC degeneration, we intravitreally injected NMDA. Briefly, Ctr and Glia-KO mice were anesthetized, and a small incision was made 0.5 to 1.0 mm behind the limbus using a 30-gauge needle. NMDA (2 μl at 100 μM in saline) was injected intravitreally. Changes in numbers of $Rbpms^+$ RGCs were quantified at 7 days after injection.

Primary cultured ON astrocytes

The ON was isolated from newborn mice and digested in 0.1% trypsin-EDTA at 37°C for 10 min. Cells were then dispersed by trituration through a pipette and cultured in a plastic dish or eight-well chamber slide [in Dulbecco's modified Eagle's medium supplemented with 5% fetal bovine serum, 5% horse serum, penicillin (10 U/ml), and streptomycin (10 μg/ml)]. Cultures were incubated with clodronate (50 μg/ml) for 5 days to eliminate microglia. Cells were maintained under 10% CO_2 at 37°C, and the culture medium was changed every 3 days. All in vitro experiments were replicated at least three times.

Statistics

Statistical analysis was performed using Origin Pro (OriginLab, Northampton, MA, USA). The *n* number means biological replicates. Data are expressed as means ± SEM. Mann-Whitney *U* tests were used for comparisons of two groups. One-way analysis of variance followed by Fisher's least significant difference test was applied for multiple comparisons. Differences were considered significant when the *P* value was less than 5%.

Study approval

All animals included in this study were obtained, housed, cared for, and used in accordance with "Guiding Principles in the Care and Use of Animals in the Field of Physiological Sciences" published by The Physiological Society of Japan. Approval was obtained from the Animal Care Committee of Yamanashi University (Chuo, Yamanashi, Japan) and the U.K. Home Office Animal Project License (University College London, London, UK).

SUPPLEMENTARY MATERIALS

Supplementary material for this article is available at https://science.org/doi/10.1126/sciadv.abq1081

View/request a protocol for this paper from *Bio-protocol*.

REFERENCES AND NOTES

1. R. N. Weinreb, T. Aung, F. A. Medeiros, The pathophysiology and treatment of glaucoma: A review. *JAMA* **311**, 1901–1911 (2014).
2. R. N. Weinreb, C. K. S. Leung, J. G. Crowston, F. A. Medeiros, D. S. Friedman, J. L. Wiggs, K. R. Martin, Primary open-angle glaucoma. *Nat. Rev. Dis. Primers.* **2**, 16067 (2016).
3. Y. Chen, Y. Lin, E. N. Vithana, L. Jia, X. Zuo, T. Y. Wong, L. J. Chen, X. Zhu, P. O. S. Tam, B. Gong, S. Qian, Z. Li, X. Liu, B. Mani, Q. Luo, C. Guzman, C. K. S. Leung, X. Li, W. Cao, Q. Yang, C. C. Y. Tham, Y. Cheng, X. Zhang, N. Wang, T. Aung, C. C. Khor, C. P. Pang, X. Sun, Z. Yang, Common variants near ABCA1 and in PMM2 are associated with primary open-angle glaucoma. *Nat. Genet.* **46**, 1115–1119 (2014).
4. P. Gharahkhani, K. P. Burdon, R. Fogarty, S. Sharma, A. W. Hewitt, S. Martin, M. H. Law, K. Cremin, J. N. C. Bailey, S. J. Loomis, L. R. Pasquale, J. L. Haines, M. A. Hauser, A. C. Viswanathan, P. McGuffin, F. Topouzis, P. J. Foster, S. L. Graham, R. J. Casson, M. Chehade, A. J. White, T. Zhou, E. Souzeau, J. Landers, J. T. Fitzgerald, S. Klebe, J. B. Ruddle, I. Goldberg, P. R. Healey; Wellcome Trust Case Control Consortium 2; NEIGHBORHOOD consortium, R. A. Mills, J. J. Wang, G. W. Montgomery, N. G. Martin, G. RadfordSmith, D. C. Whiteman, M. A. Brown, J. L. Wiggs, D. A. Mackey, P. Mitchell, S. MacGregor, J. E. Craig, Common variants near ABCA1, AFAP1 and GMDS confer risk of primary open-angle glaucoma. *Nat. Genet.* **46**, 1120–1125 (2014).
5. P. G. Hysi, C.-Y. Cheng, H. Springelkamp, S. Macgregor, J. N. C. Bailey, R. Wojciechowski, V. Vitart, A. Nag, A. W. Hewitt, R. Höhn, C. Venturini, A. Mirshahi, W. D. Ramdas, G. Thorleifsson, E. Vithana, C.-C. Khor, A. B. Stefansson, J. Liao, J. L. Haines, N. Amin, Y. X. Wang, P. S. Wild, A. B. Ozel, J. Z. Li, B. W. Fleck, T. Zeller, S. E. Staffieri, Y.-Y. Teo, G. Cuellar-Partida, X. Luo, R. R. Allingham, J. E. Richards, A. Senft, L. C. Karssen, Y. Zheng, C. Bellenguez, L. Xu, A. I. Iglesias, J. F. Wilson, J. H. Kang, E. M. van Leeuwen, V. Jonsson, U. Thorsteinsdottir, D. D. G. Despriet, S. Ennis, S. E. Moroi, N. G. Martin, N. M. Jansonius, S. Yazar, E.-S. Tai, P. Amouyel, J. Kirwan, L. M. E. van Koolwijk, M. A. Hauser, F. Jonasson, P. Leo, S. J. Loomis, R. Fogarty, F. Rivadeneira, L. Kearns, K. J. Lackner, P. T. V. M. de Jong, C. L. Simpson, C. E. Pennell, B. A. Oostra, A. G. Uitterlinden, S.-M. Saw, A. J. Lotery, J. E. Bailey-Wilson, A. Hofman, J. R. Vingerling, C. Maubaret, N. Pfeiffer, R. C. W. Wolfs, H. G. Lemij, T. L. Young, L. R. Pasquale, C. Delcourt, T. D. Spector, C. C. W. Klaver, K. S. Small, K. P. Burdon, K. Stefansson, T.-Y. Wong; BMES GWAS Group; NEIGHBORHOOD Consortium; Wellcome Trust Case Control Consortium 2, A. Viswanathan, D. A. Mackey, J. E. Craig, J. L. Wiggs, C. M. van Duijn, C. J. Hammond, T. Aung, Genome-wide analysis of multi-ancestry cohorts identifies new loci influencing intraocular pressure and susceptibility to glaucoma. *Nat. Genet.* **46**, 1126–1130 (2014).

6. A. P. Khawaja, J. N. C. Bailey, N. J. Wareham, R. A. Scott, M. Simcoe, R. P. Igo Jr., Y. E. Song, R. Wojciechowski, C.-Y. Cheng, P. T. Khaw, L. R. Pasquale, J. L. Haines, P. J. Foster, J. L. Wiggs, C. J. Hammond, P. G. Hysi; UK Biobank Eye and Vision Consortium; NEIGHBORHOOD Consortium, Genome-wide analyses identify 68 new loci associated with intraocular pressure and improve risk prediction for primary open-angle glaucoma. *Nat. Genet.* **50**, 778–782 (2018).
7. Y. Hamon, C. Broccardo, O. Chambenoit, M. F. Luciani, F. Toti, S. Chaslin, J. M. Freyssinet, P. F. Devaux, J. McNeish, D. Marguet, G. Chimini, ABC1 promotes engulfment of apoptotic cells and transbilayer redistribution of phosphatidylserine. *Nat. Cell Biol.* **2**, 399–406 (2000).
8. Y. M. Morizawa, Y. Hirayama, N. Ohno, S. Shibata, E. Shigetomi, Y. Sui, J. Nabekura, K. Sato, F. Okajima, H. Takebayashi, H. Okano, S. Koizumi, Reactive astrocytes function as phagocytes after brain ischemia via ABCA1-mediated pathway. *Nat. Commun.* **8**, 28 (2017).
9. B. Castella, J. Kopecka, P. Sciancalepore, G. Mandili, M. Foglietta, N. Mitro, D. Caruso, F. Novelli, C. Riganti, M. Massaia, The ATP-binding cassette transporter A1 regulates phosphoantigen release and Vγ9Vδ2 T cell activation by dendritic cells. *Nat. Commun.* **8**, 15663 (2017).
10. X. Zha, J. Genest Jr., R. McPherson, Endocytosis is enhanced in Tangier fibroblasts: Possible role of ATP-binding cassette protein A1 in endosomal vesicular transport. *J. Biol. Chem.* **276**, 39476–39483 (2001).
11. X. Bi, C. Vitali, M. Cuchel, ABCA1 and inflammation: From animal models to humans. *Arterioscler. Thromb. Vasc. Biol.* **35**, 1551–1553 (2015).
12. C. Tang, Y. Liu, P. S. Kessler, A. M. Vaughan, J. F. Oram, The macrophage cholesterol exporter ABCA1 functions as an anti-inflammatory receptor. *J. Biol. Chem.* **284**, 32336–32343 (2009).
13. J. F. Oram, J. W. Heinecke, ATP-binding cassette transporter A1: A cell cholesterol exporter that protects against cardiovascular disease. *Physiol. Rev.* **85**, 1343–1372 (2005).
14. Y. Shinozaki, K. Shibata, K. Yoshida, E. Shigetomi, C. Gachet, K. Ikenaka, K. F. Tanaka, S. Koizumi, Transformation of astrocytes to a neuroprotective phenotype by microglia via P2Y1 receptor downregulation. *Cell Rep.* **19**, 1151–1164 (2017).
15. H. Chun, H. Im, Y. J. Kang, Y. Kim, J. H. Shin, W. Won, J. Lim, Y. Ju, Y. M. Park, S. Kim, S. E. Lee, J. Lee, J. Woo, Y. Hwang, H. Cho, S. Jo, J. H. Park, D. Kim, D. Y. Kim, J. S. Seo, B. J. Gwag, Y. S. Kim, K. D. Park, B. K. Kaang, H. Cho, H. Ryu, C. J. Lee, Severe reactive astrocytes precipitate pathological hallmarks of Alzheimer's disease via H2O2(−) production. *Nat. Neurosci.* **23**, 1555–1566 (2020).
16. Y. H. Ju, M. Bhalla, S. J. Hyeon, J. E. Oh, S. Yoo, U. Chae, J. Kwon, W. Koh, J. Lim, Y. M. Park, J. Lee, I. J. Cho, H. Lee, H. Ryu, C. J. Lee, Astrocytic urea cycle detoxifies Aβ-derived ammonia while impairing memory in Alzheimer's disease. *Cell Metab.* **34**, 1104–1120.e8 (2022).
17. S. A. Liddelow, K. A. Guttenplan, L. E. Clarke, F. C. Bennett, C. J. Bohlen, L. Schirmer, M. L. Bennett, A. E. Munch, W. S. Chung, T. C. Peterson, D. K. Wilton, A. Frouin, B. A. Napier, N. Panicker, M. Kumar, M. S. Buckwalter, D. H. Rowitch, V. L. Dawson, T. M. Dawson, B. Stevens, B. A. Barres, Neurotoxic reactive astrocytes are induced by activated microglia. *Nature* **541**, 481–487 (2017).
18. N. J. Maragakis, J. D. Rothstein, Mechanisms of disease: Astrocytes in neurodegenerative disease. *Nat. Clin. Pract. Neurol.* **2**, 679–689 (2006).
19. K. A. Guttenplan, B. K. Stafford, R. N. El-Danaf, D. I. Adler, A. E. Munch, M. K. Weigel, A. D. Huberman, S. A. Liddelow, Neurotoxic reactive astrocytes drive neuronal death after retinal injury. *Cell Rep.* **31**, 107776 (2020).
20. Y. Shinozaki, S. Koizumi, Potential roles of astrocytes and Müller cells in the pathogenesis of glaucoma. *J. Pharmacol. Sci.* **145**, 262–267 (2021).
21. E. Vecino, F. D. Rodriguez, N. Ruzafa, X. Pereiro, S. C. Sharma, Glia-neuron interactions in the mammalian retina. *Prog. Retin. Eye Res.* **51**, 1–40 (2016).
22. R. F. Gariano, E. H. Sage, H. J. Kaplan, A. E. Hendrickson, Development of astrocytes and their relation to blood vessels in fetal monkey retina. *Invest. Ophthalmol. Vis. Sci.* **37**, 2367–2375 (1996).
23. J. M. Ramirez, A. Trivino, A. I. Ramirez, J. J. Salazar, J. Garcia-Sanchez, Structural specializations of human retinal glial cells. *Vision Res.* **36**, 2029–2036 (1996).
24. G. R. Howell, R. T. Libby, T. C. Jakobs, R. S. Smith, F. C. Phalan, J. W. Barter, J. M. Barbay, J. K. Marchant, N. Mahesh, V. Porciatti, A. V. Whitmore, R. H. Masland, S. W. M. John, Axons of retinal ganglion cells are insulted in the optic nerve early in DBA/2J glaucoma. *J. Cell Biol.* **179**, 1523–1537 (2007).
25. M. R. Hernandez, The optic nerve head in glaucoma: Role of astrocytes in tissue remodeling. *Prog. Retin. Eye Res.* **19**, 297–321 (2000).
26. A. Trivino, J. M. Ramirez, J. J. Salazar, A. I. Ramirez, J. Garcia-Sanchez, Immunohistochemical study of human optic nerve head astroglia. *Vision Res.* **36**, 2015–2028 (1996).
27. H. A. Quigley, E. M. Addicks, Chronic experimental glaucoma in primates. II. Effect of extended intraocular pressure elevation on optic nerve head and axonal transport. *Invest. Ophthalmol. Vis. Sci.* **19**, 137–152 (1980).
28. M. R. Hernandez, J. D. Pena, The optic nerve head in glaucomatous optic neuropathy. *Arch. Ophthalmol.* **115**, 389–395 (1997).
29. M. L. Cooper, J. W. Collyer, D. J. Calkins, Astrocyte remodeling without gliosis precedes optic nerve axonopathy. *Acta Neuropathol. Commun.* **6**, 38 (2018).
30. B. A. Rheaume, A. Jereen, M. Bolisetty, M. S. Sajid, Y. Yang, K. Renna, L. Sun, P. Robson, E. F. Trakhtenberg, Single cell transcriptome profiling of retinal ganglion cells identifies cellular subtypes. *Nat. Commun.* **9**, 2759 (2018).
31. N. M. Tran, K. Shekhar, I. E. Whitney, A. Jacobi, I. Benhar, G. Hong, W. Yan, X. Adiconis, M. E. Arnold, J. M. Lee, J. Z. Levin, D. Lin, C. Wang, C. M. Lieber, A. Regev, Z. He, J. R. Sanes, Single-cell profiles of retinal ganglion cells differing in resilience to injury reveal neuroprotective genes. *Neuron* **104**, 1039–1055.e12 (2019).
32. G. R. Howell, D. G. Macalinao, G. L. Sousa, M. Walden, I. Soto, S. C. Kneeland, J. M. Barbay, B. L. King, J. K. Marchant, M. Hibbs, B. Stevens, B. A. Barres, A. F. Clark, R. T. Libby, S. W. M. John, Molecular clustering identifies complement and endothelin induction as early events in a mouse model of glaucoma. *J. Clin. Invest.* **121**, 1429–1444 (2011).
33. Y. Shinozaki, K. Kashiwagi, K. Namekata, A. Takeda, N. Ohno, B. Robaye, T. Harada, T. Iwata, S. Koizumi, Purinergic dysregulation causes hypertensive glaucoma-like optic neuropathy. *JCI Insight* **2**, (2017).
34. C. K. Leung, S. Lam, R. N. Weinreb, S. Liu, C. Ye, L. Liu, J. He, G. W. Lai, T. Li, D. S. Lam, Retinal nerve fiber layer imaging with spectral-domain optical coherence tomography: Analysis of the retinal nerve fiber layer map for glaucoma detection. *Ophthalmology* **117**, 1684–1691 (2010).
35. P. A. Williams, J. R. Tribble, K. W. Pepper, S. D. Cross, B. P. Morgan, J. E. Morgan, S. W. M. John, G. R. Howell, Inhibition of the classical pathway of the complement cascade prevents early dendritic and synaptic degeneration in glaucoma. *Mol. Neurodegener.* **11**, 26 (2016).
36. G. Chidlow, A. Ebneter, J. P. M. Wood, R. J. Casson, The optic nerve head is the site of axonal transport disruption, axonal cytoskeleton damage and putative axonal regeneration failure in a rat model of glaucoma. *Acta Neuropathol.* **121**, 737–751 (2011).
37. H. A. Quigley, D. R. Anderson, Distribution of axonal transport blockade by acute intraocular pressure elevation in the primate optic nerve head. *Invest. Ophthalmol. Vis. Sci.* **16**, 640–644 (1977).
38. H. A. Quigley, W. R. Green, The histology of human glaucoma cupping and optic nerve damage: Clinicopathologic correlation in 21 eyes. *Ophthalmology* **86**, 1803–1827 (1979).
39. T. Harada, C. Harada, K. Nakamura, H.-M. A. Quah, A. Okumura, K. Namekata, T. Saeki, M. Aihara, H. Yoshida, A. Mitani, K. Tanaka, The potential role of glutamate transporters in the pathogenesis of normal tension glaucoma. *J. Clin. Invest.* **117**, 1763–1770 (2007).
40. D. C. Hood, L. J. Frishman, S. Viswanathan, J. G. Robson, J. Ahmed, Evidence for a ganglion cell contribution to the primate electroretinogram (ERG): Effects of TTX on the multifocal ERG in macaque. *Vis. Neurosci.* **16**, 411–416 (1999).
41. D. C. Hood, V. C. Greenstein, K. Holopigian, R. Bauer, B. Firoz, J. M. Liebmann, J. G. Odel, R. Ritch, An attempt to detect glaucomatous damage to the inner retina with the multifocal ERG. *Invest. Ophthalmol. Vis. Sci.* **41**, 1570–1579 (2000).
42. S. Hasegawa, A. Ohshima, Y. Hayakawa, M. Takagi, H. Abe, Multifocal electroretinograms in patients with branch retinal artery occlusion. *Invest. Ophthalmol. Vis. Sci.* **42**, 298–304 (2001).
43. E. E. Sutter, M. A. Bearse Jr., The optic nerve head component of the human ERG. *Vision Res.* **39**, 419–436 (1999).
44. G. Chinetti, S. Lestavel, V. Bocher, A. T. Remaley, B. Neve, I. P. Torra, E. Teissier, A. Minnich, M. Jaye, N. Duverger, H. B. Brewer, J. C. Fruchart, V. Clavey, B. Staels, PPAR-alpha and PPAR-gamma activators induce cholesterol removal from human macrophage foam cells through stimulation of the ABCA1 pathway. *Nat. Med.* **7**, 53–58 (2001).
45. M. Kanehisa, M. Araki, S. Goto, M. Hattori, M. Hirakawa, M. Itoh, T. Katayama, S. Kawashima, S. Okuda, T. Tokimatsu, Y. Yamanishi, KEGG for linking genomes to life and the environment. *Nucleic Acids Res.* **36**, D480–D484 (2008).
46. N. J. Sucher, K. Kohler, L. Tenneti, H.-K. Wong, T. Gründer, S. Fauser, T. Wheeler-Schilling, N. Nakanishi, S. A. Lipton, E. Guenther, N-methyl-D-aspartate receptor subunit NR3A in the retina: Developmental expression, cellular localization, and functional aspects. *Invest. Ophthalmol. Vis. Sci.* **44**, 4451–4456 (2003).
47. I. Perez-Otano, R. S. Larsen, J. F. Wesseling, Emerging roles of GluN3-containing NMDA receptors in the CNS. *Nat. Rev. Neurosci.* **17**, 623–635 (2016).
48. N. Nakanishi, S. Tu, Y. Shin, J. Cui, T. Kurokawa, D. Zhang, H.-S. Chen, G. Tong, S. A. Lipton, Neuroprotection by the NR3A subunit of the NMDA receptor. *J. Neurosci.* **29**, 5260–5265 (2009).
49. K. Hamada, Y. Shinozaki, K. Namekata, M. Matsumoto, N. Ohno, T. Segawa, K. Kashiwagi, T. Harada, S. Koizumi, Loss of $P2Y_1$ receptors triggers glaucoma-like pathology in mice. *Br. J. Pharmacol.* **178**, 4552–4571 (2021).
50. J. Luo, S. Wang, Z. Zhou, Y. Zhao, Ad- and AAV8-mediated ABCA1 gene therapy in a murine model with retinal ischemia/reperfusion injuries. *Mol. Ther. Methods Clin. Dev.* **20**, 551–558 (2021).

51. M. Karlsson, C. Zhang, L. Mear, W. Zhong, A. Digre, B. Katona, E. Sjostedt, L. Butler, J. Odeberg, P. Dusart, F. Edfors, P. Oksvold, K. von Feilitzen, M. Zwahlen, M. Arif, O. Altay, X. Li, M. Ozcan, A. Mardinoglu, L. Fagerberg, J. Mulder, Y. Luo, F. Ponten, M. Uhlen, C. Lindskog, A single-cell type transcriptomics map of human tissues. *Sci. Adv.* **7**, 1275 (2021).
52. S. W. Lukowski, C. Y. Lo, A. A. Sharov, Q. Nguyen, L. Fang, S. S. Hung, L. Zhu, T. Zhang, U. Grünert, T. Nguyen, A. Senabouth, J. S. Jabbari, E. Welby, J. C. Sowden, H. S. Waugh, A. Mackey, G. Pollock, T. D. Lamb, P.-Y. Wang, A. W. Hewitt, M. C. Gillies, J. E. Powell, R. C. Wong, A single-cell transcriptome atlas of the adult human retina. *EMBO J.* **38**, e100811 (2019).
53. K. Bowden, N. D. Ridgway, OSBP negatively regulates ABCA1 protein stability. *J. Biol. Chem.* **283**, 18210–18217 (2008).
54. D. Yan, M. I. Mayranpaa, J. Wong, J. Perttila, M. Lehto, M. Jauhiainen, P. T. Kovanen, C. Ehnholm, A. J. Brown, V. M. Olkkonen, OSBP-related protein 8 (ORP8) suppresses ABCA1 expression and cholesterol efflux from macrophages. *J. Biol. Chem.* **283**, 332–340 (2008).
55. N. Ban, T. J. Lee, A. Sene, Z. Dong, A. Santeford, J. B. Lin, D. S. Ory, R. S. Apte, Disrupted cholesterol metabolism promotes age-related photoreceptor neurodegeneration. *J. Lipid Res.* **59**, 1414–1423 (2018).
56. Y. Lei, N. Garrahan, B. Hermann, M. P. Fautsch, D. H. Johnson, M. R. Hernandez, M. Boulton, J. E. Morgan, Topography of neuron loss in the retinal ganglion cell layer in human glaucoma. *Br. J. Ophthalmol.* **93**, 1676–1679 (2009).
57. J. Bradford, J. Y. Shin, M. Roberts, C. E. Wang, X. J. Li, S. Li, Expression of mutant huntingtin in mouse brain astrocytes causes age-dependent neurological symptoms. *Proc. Natl. Acad. Sci. U.S.A.* **106**, 22480–22485 (2009).
58. K. Yamanaka, S. J. Chun, S. Boillee, N. Fujimori-Tonou, H. Yamashita, D. H. Gutmann, R. Takahashi, H. Misawa, D. W. Cleveland, Astrocytes as determinants of disease progression in inherited amyotrophic lateral sclerosis. *Nat. Neurosci.* **11**, 251–253 (2008).
59. D. Sun, M. Lye-Barthel, R. H. Masland, T. C. Jakobs, The morphology and spatial arrangement of astrocytes in the optic nerve head of the mouse. *J. Comp. Neurol.* **516**, 1–19 (2009).
60. A. Ito, C. Hong, X. Rong, X. Zhu, E. J. Tarling, P. N. Hedde, E. Gratton, J. Parks, P. Tontonoz, LXRs link metabolism to inflammation through Abca1-dependent regulation of membrane composition and TLR signaling. *eLife* **4**, e08009 (2015).
61. M. Valenza, E. Cattaneo, Emerging roles for cholesterol in Huntington's disease. *Trends Neurosci.* **34**, 474–486 (2011).
62. A. O. Sodero, J. Vriens, D. Ghosh, D. Stegner, A. Brachet, M. Pallotto, M. Sassoe-Pognetto, J. F. Brouwers, J. B. Helms, B. Nieswandt, T. Voets, C. G. Dotti, Cholesterol loss during glutamate-mediated excitotoxicity. *EMBO J.* **31**, 1764–1773 (2012).
63. D. H. Mauch, K. Nagler, S. Schumacher, C. Goritz, E. C. Muller, A. Otto, F. W. Pfrieger, CNS synaptogenesis promoted by glia-derived cholesterol. *Science* **294**, 1354–1357 (2001).
64. G. Tezel, L. Y. Li, R. V. Patil, M. B. Wax, TNF-alpha and TNF-alpha receptor-1 in the retina of normal and glaucomatous eyes. *Invest. Ophthalmol. Vis. Sci.* **42**, 1787–1794 (2001).
65. A. Denoyer, D. Godefroy, I. Celerier, J. Frugier, J. Degardin, J. K. Harrison, F. Brignole-Baudouin, S. Picaud, F. Baleux, J. A. Sahel, W. Rostene, C. Baudouin, CXCR3 antagonism of SDF-1(5-67) restores trabecular function and prevents retinal neurodegeneration in a rat model of ocular hypertension. *PLOS ONE* **7**, e37873 (2012).
66. A. Pantalon, O. Obada, D. Constantinescu, C. Feraru, D. Chiselita, Inflammatory model in patients with primary open angle glaucoma and diabetes. *Int. J. Ophthalmol.* **12**, 795–801 (2019).
67. K. Zhang, G. A. McQuibban, C. Silva, G. S. Butler, J. B. Johnston, J. Holden, I. Clark-Lewis, C. M. Overall, C. Power, HIV-induced metalloproteinase processing of the chemokine stromal cell derived factor-1 causes neurodegeneration. *Nat. Neurosci.* **6**, 1064–1071 (2003).
68. A. E. Bochem, F. M. van der Valk, S. Tolani, E. S. Stroes, M. Westerterp, A. R. Tall, Increased systemic and plaque inflammation in *ABCA1* mutation carriers with attenuation by statins. *Arterioscl. Throm. Vas.* **35**, 1663–1669 (2015).
69. H.-P. Liu, W.-Y. Lin, S.-H. Liu, W.-F. Wang, C.-H. Tsai, B.-T. Wu, C.-K. Wang, F.-J. Tsai, Genetic variation in N-methyl-D-aspartate receptor subunit NR3A but not NR3B influences susceptibility to Alzheimer's disease. *Dement. Geriatr. Cogn. Disord.* **28**, 521–527 (2009).
70. D. L. Rousso, M. Qiao, R. D. Kagan, M. Yamagata, R. D. Palmiter, J. R. Sanes, Two pairs of ON and OFF retinal ganglion cells are defined by intersectional patterns of transcription factor expression. *Cell Rep.* **15**, 1930–1944 (2016).
71. K. B. VanderWall, B. Lu, J. S. Alfaro, A. R. Allsop, A. S. Carr, S. Wang, J. S. Meyer, Differential susceptibility of retinal ganglion cell subtypes in acute and chronic models of injury and disease. *Sci. Rep.* **10**, 17359 (2020).
72. J. Wu, M. Coffey, A. Reidy, R. Wormald, Impaired motion sensitivity as a predictor of subsequent field loss in glaucoma suspects: The Roscommon Glaucoma Study. *Br. J. Ophthalmol.* **82**, 534–537 (1998).
73. W. A. Hare, E. WoldeMussie, R. K. Lai, H. Ton, G. Ruiz, T. Chun, L. Wheeler, Efficacy and safety of memantine treatment for reduction of changes associated with experimental glaucoma in monkey, I: Functional measures. *Invest. Ophthalmol. Vis. Sci.* **45**, 2625–2639 (2004).
74. M. Kaul, S. A. Lipton, Chemokines and activated macrophages in HIV gp120-induced neuronal apoptosis. *Proc. Natl. Acad. Sci. U.S.A.* **96**, 8212–8216 (1999).
75. V. Musante, F. Longordo, E. Neri, M. Pedrazzi, F. Kalfas, P. Severi, M. Raiteri, A. Pittaluga, RANTES modulates the release of glutamate in human neocortex. *J. Neurosci.* **28**, 12231–12240 (2008).
76. A. B. Sanchez, K. E. Medders, R. Maung, P. Sanchez-Pavon, D. Ojeda-Juarez, M. Kaul, CXCL12-induced neurotoxicity critically depends on NMDA receptor-gated and L-type Ca^{2+} channels upstream of p38 MAPK. *J. Neuroinflammation* **13**, 252 (2016).
77. R. N. Weinreb, J. M. Liebmann, G. A. Cioffi, I. Goldberg, J. D. Brandt, C. A. Johnson, L. M. Zangwill, S. Schneider, H. Badger, M. Bejanian, Oral memantine for the treatment of glaucoma: Design and results of 2 randomized, placebo-controlled, phase 3 studies. *Ophthalmology* **125**, 1874–1885 (2018).

Acknowledgments: We thank Y. Watanabe, Y. Fukasawa, and Y. Koseki from the Department of Neuropharmacology, Interdisciplinary Graduate School of Medicine, University of Yamanashi. We also thank the laboratory members. We are grateful to J. S. Parks (Wake Forest University), J. Karasinska, and M. R. Hayden (British Columbia, Canada) for providing $ABCA1^{flox/flox}$::GFAP-Cre mice. We also thank F. Okajima (Gunma University, Japan) for providing ABCA1-KO mice. We thank A. Limb, P. Khaw, A. Khawaja, and N. Pontikos (UCL Institute of Ophthalmology) for the critical reading of this manuscript. We thank L. Kreiner from Edanz (https://jp.edanz.com/ac) for editing a draft of this manuscript. **Funding:** This study was supported by the Takeda Science Foundation (Y.S., T.H., and S.K.); Mitsubishi Foundation (S.K.); Japan Agency for Medical Research and Development (grant number 20gm1310008s0101 to S.K.); Japan Society for the Promotion of Science KAKENHI grant numbers JP16K18390 (Y.S.), JP18K06481 (Y.S.), JP20KK0366 (Y.S.), JP20K07751 (K.N.), JP19KK0229 (T.H.), JP21H02819 (K.N. and T.H.), JP21K18279 (K.N. and T.H.), JP16H06280 (N.O.), JP16H04669 (S.K.), JP25117003 (S.K.), JP18H05121 (S.K.), JP19H04746 (S.K.), JP20H05902 (Y.S., E.S., and S.K.), JP20H05984 (S.K.), and JP21H04786 (Y.S., K.K., T.H., and S.K.); Core-to-Core Program (JPJSCCA20180008) (S.K.), Cooperative Research Program of the "Network Joint Research Center for Materials and Devices" (N.O.); and a Grant-in-Aid for Scientific Research on Innovative Areas-Resource and Technical Support Platforms for Promoting Research "Advanced Bioimaging Support" (JP16H06280) (Y.S. and N.O.). This study was also partially supported by JST Grant CREST number JPMJCR14G2 (S.K.), AMED-CREST grant number JP20gm131000 (S.K.), a Santen SenSyT studentship (A.L. and S.-i.O.), a Frontier Project Grant from the University of Yamanashi (S.K.), and a grant from Moorfields Eye Charity (S.-i.O., grant number MEC1601A). **Author contributions:** Y.S. designed, performed, and analyzed the experiments described in each figure and wrote the manuscript. A.L. and S.-i.O. designed and performed all scRNA-seq experiments and bioinformatics analyses and wrote the manuscript. K.N. and T.H. performed mfERGs and analyzed the data. A.T., Y.D., F. S., Y.M.M., and E.S. performed the experiments described in some figures. S.S., H.B.N., and N.O. performed SBF-SEM and analyzed the data. T.S. and K.M. performed bulk RNA-seq experiments and analysis. N.Y. and H.T. performed and analyzed in situ hybridization. K.K., S.-i.O., and S.K. coordinated the project, analyzed the data, and cowrote the manuscript. The order of the two co–first authors was determined on the basis of the scope of their respective contributions. **Competing interests:** Y.S., K.K., and S.K. are inventors on a patent related to this work filed by the University of Yamanashi (no. P2018-115732, filed 19 June 2018, published 26 December 2019). The authors declare that they have no other competing interests. **Data and materials availability:** The dataset used in the present study is available through the NCBI GEO accession [GSE207930 (//0-www-ncbi-nlm-nih-gov.brum.beds.ac.uk/geo/query/acc.cgi?acc=GSE207930), GSE207928 (//0-www-ncbi-nlm-nih-gov.brum.beds.ac.uk/geo/query/acc.cgi?acc=GSE207928), and GSE207929 (//0-www-ncbi-nlm-nih-gov.brum.beds.ac.uk/geo/query/acc.cgi?acc=GSE207929)]. The $ABCA1^{flox/flox}$::GFAP-Cre mouse can be provided by M. R. Hayden pending scientific review and a completed material transfer agreement. Request for the $ABCA1^{flox/flox}$::GFAP-Cre mouse should be submitted to the University of British Columbia. The ABCA1-KO mouse can be provided by the Jackson Laboratory pending scientific review and a completed material transfer agreement. Request for the ABCA1-KO mouse should be submitted to the Jackson Laboratory. The information on the *Abca1* gene for preparing in situ hybridization is available at NCBI (GenBank accession number NM_013454, full length: 1 to 6786 nt). All data needed to evaluate the conclusions in the paper are present in the paper and/or the Supplementary Materials.

Submitted 18 March 2022
Accepted 16 September 2022
Published 4 November 2022
10.1126/sciadv.abq1081